A fast boundary element method using the Z-transform and high-frequency approximations for large-scale 3D transient wave problems

Damien Mavaleix-Marchessoux, Marc Bonnet, Stéphanie Chaillat, Bruno Leblé

Received: Added at production | Revised: Added at production | Accepted: Added at production

DOI: xxx/xxxx

RESEARCH ARTICLE

A fast BEM procedure using the Z-transform and high-frequency approximations for large-scale 3D transient wave problems

Damien Mavaleix-Marchessoux[1,2] | Marc Bonnet[1] | Stéphanie Chaillat[1] | Bruno Leblé[2]

[1]POEMS (CNRS-ENSTA-INRIA), ENSTA Paris, 91120 Palaiseau, France
[2]Naval Group Research, Technocampus Ocean, 44430 Bouguenais, France

Correspondence
*Stéphanie Chaillat. Email: stephanie.chaillat@ensta-paris.fr

Abstract

3D rapid transient acoustic problems are difficult to solve numerically when dealing with large geometries, because numerical methods based on geometry discretisation (mesh), such as the boundary element method (BEM) or the finite element method (FEM), often require to solve a linear system (from the spacial discretisation) for each time step. We propose a numerical method to efficiently deal with 3D rapid transient acoustic problems set in large exterior domains. Using the $\mathcal{Z}$-transform and the convolution quadrature method (CQM), we first present a straightforward way to reframe the problem to the solving of a large amount (the number of time steps, M) of frequency-domain BEMs. Then, taking advantage of a well-designed high-frequency approximation (HFA), we drastically reduce the number of frequency-domain BEMs to be solved, with little loss of accuracy. The complexity of the resulting numerical procedure turns out to be $O(1)$ in regards to the time discretisation and $O(N \log N)$ for the spacial discretisation, the latter being prescribed by the complexity of the used fast BEM solver.

Examples of applications are proposed to illustrate the efficiency of the procedure in the case of fluid-structure interaction: the radiation of an acoustic wave into a fluid by a deformable structure with prescribed velocity, and the scattering of an abrupt wave by simple and realistic geometries.

KEYWORDS:
Fast BEMs; Convolution Quadrature Method; Helmholtz; fluid-structure problems

1 | INTRODUCTION

Submarines must withstand the effects of rapid dynamic loads induced by underwater explosions. This lends great importance on the numerical simulation of the effects of a remote underwater blast on a given structure (see Fig. 1), in view of the very high cost of full-scale experimental testing. A remote underwater explosion is a complex event[1,2] that has two distinct effects: it sends a shock wave, then creates an oscillating bubble of gas that sets water in slower motion. The two phenomena have quite different characteristics and time scales. The shock wave initially sent by the blast can be modelled in the structure vicinity by the theory of linear acoustics, whereas the incompressible potential flow model is adequate for the delayed and slower perturbation induced by the oscillating bubble. We assume the blast to be remote enough to allow temporal separation of the two phenomena as experienced by the ship. Our overall goal is to develop, under these conditions, a computational solution methodology for the fluid-structure interaction (FSI) problem taking into account both phenomena.

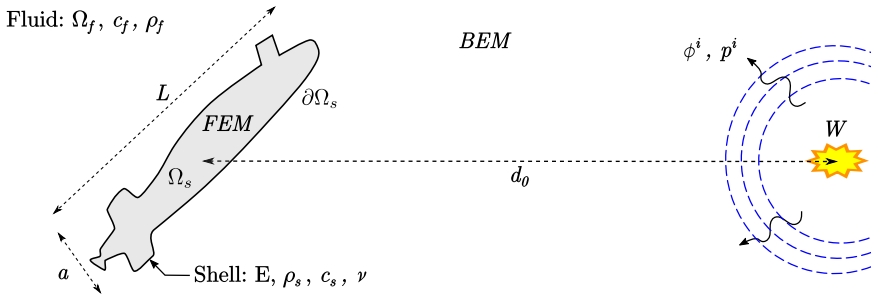

FIGURE 1 Submarine experiencing a remote underwater blast.

This work focuses on one component of that global treatment, namely the computation of transient acoustic fields induced by the shock wave of the blast on a submarine whose motion is given. The acoustic domain (the ocean) is assumed to be unbounded, i.e., reflections of the shock wave by the free surface (water surface) and the seabed are disregarded. The water is treated as a homogeneous, isotropic and inviscid fluid in which flows are irrotational.

Domain discretisation methods such as the FEM are viable approaches for the acoustic component of the computation, and indeed are used for the present type of applications in e.g.,[3]. However, they require large amounts of degrees of freedom, and geometrical details of the complex submarine surface entail meshing difficulties, especially for the fluid domain. On the other hand, the boundary element method (BEM)[4], based on the discretisation of boundary integral equations (BIEs), only requires in the present context the discretisation of the submarine wet surface and is very well suited to the presently-adopted modelling assumptions for the fluid domain.

Due to the inherently transient nature of the shock wave phenomenon, the resulting acoustic field must be computed in the time domain. The classical approach for the numerical solution of BIEs in the time domain, known as retarded potential BIEs, exploits a direct space-time discretisation[5,6,7,8,9,10,11]. It is delicate to implement because the fundamental solutions couple the space and time variables through the retarded time, making the accurate evaluation of space-time element integrals quite technical and intricate. Moreover, retarded potential BEMs may experience numerical instabilities related to the choice of the time step. These difficulties can be sidestepped by resorting to the more-recently developed approach based on the convolution quadrature method (CQM)[12,13], which deals with transient problems by exploiting the time convolution structure of time-domain BIEs and combining suitably defined BEM solutions obtained in the complex frequency domain[14,15,16,17,18]. CQM-based solution algorithms, which are becoming the mainstream approach for solving time domain BIEs, can therefore rely on the relative simplicity of frequency-domain BEMs and the availability of existing robust and efficient BEM codes. Most importantly, applications underlying this work need accelerated BEMs, which for frequency-domain BIEs have been extensively studied and allow to efficiently deal with large-scale time-harmonic problems, even at high frequencies[19,20,21,22,23]. Hence, adopting the CQM framework allows to take direct advantage of fast frequency-domain BEMs in dealing with transient rapid problems. Fast BEMs for retarded potential BIEs[24,25] are comparatively harder to formulate, and thus less widespread.

This article focuses on the boundary element methodology for solving the transient acoustic problems involved in the intended FSI analyses, for which we adopt the CQM framework. Since its inception[12] and consistently with practice, the CQM emphasizes the discrete-time setting. As the time-discrete analog of the Laplace transform[26], the $\mathcal{Z}$-transform and its inversion formula can then naturally be given a prominent role for setting up transient BEM formulations, a viewpoint appearing in[27] and also exploited in[15]. We present here a self-contained derivation, based on the $\mathcal{Z}$-transform, of the time-discrete transient BEM formulation which we henceforth choose to call the $\mathcal{Z}$-BEM. We moreover focus on problems where the numbers N of spatial degrees of freedom (DOFs) and M of time steps are both large. The large-DOF aspect is addressed by applying the fast multipole method (FMM) to the frequency-domain boundary integral equations (BIEs) arising in the $\mathcal{Z}$-BEM; other approaches such as $\mathcal{H}$-matrix compression would also be applicable. Indeed, the ability of resorting to well-established fast BEM methodologies for (complex) frequency-domain problems is among the definite advantages of CQM- or $\mathcal{Z}$-transform-based BEMs. Then, large numbers M of time steps may also overwhelm available computational resources, as the $\mathcal{Z}$-BEM (or more generally the CQM-BEM) *a priori* requires $O(M)$ BEM solutions in the frequency domain. To address this issue, we propose to resort to a (largely heuristic) high-frequency approximation (HFA) for all BEM problems at frequencies above a certain threshold. In particular, we show that the availability and exploitation of a HFA reduces the BEM solution burden to $O(1)$ for given N. We demonstrate the usefulness and efficiency of our fast $\mathcal{Z}$-BEM treatment incorporating the FMM and the HFA on examples having reference solutions, and

then on a submarine-shaped geometry with $N \approx 3\ 10^6$ and $M = 10^4$. Another approach having a $O(1)$ time complexity has recently been proposed[28]. Its computational gain is based on a band-limited representation of long time signals, a premise which does not readily fit our target industrial studies featuring discontinuous incident waves. Alternatively, as pointed out in[14], many of the frequency-domain BEM problems can simply be disregarded if, unlike in this study, the boundary data is smooth and time-limited.

This article is organised as follows. In Sec. 2, the CQM is shown to convert time-domain BIEs into a family of frequency-domain BEM problems governing the $\mathcal{Z}$-transforms of boundary fields, a viewpoint that has the extra advantage of allowing a simple and concise derivation of the resulting $\mathcal{Z}$-BEM within the standard BIE formalism. The section ends with a summary of known basics of the frequency domain BEM and its acceleration by the FMM. Our proposed HFA-based improvement for dealing efficiently with rapid transient wave propagation problems is then presented in Sec. 3. In Sec. 4, we evaluate the resulting accelerated $\mathcal{Z}$-BEM against reference solutions on two examples (radiation by a pulsating sphere, scattering of a spherical wave by an infinite cylinder). Finally, we show in Sec. 5 that we are able to deal with the scattering by a full-scale submarine of a wave emerging from an underwater blast, one of the main computational tasks involved in our challenging industrial modelling goal.

2 | $\mathcal{Z}$-BEM FOR 3D TRANSIENT ACOUSTIC PROBLEMS

2.1 | Transient wave propagation problems.

We consider transient linear wave propagation problems in an exterior acoustic domain of the form $\Omega = \mathbb{R}^3 \setminus \overline{\Omega_s}$, where Ω_s denotes a bounded domain with regular boundary Γ. Assuming the fluid to be at initial rest, the problems of interest have the form:

$$\text{Find } \psi \text{ such that } \begin{cases} \Delta\psi - \dfrac{1}{c^2}\dfrac{\partial^2\psi}{\partial t^2} = 0 & (\mathbf{x},t) \in \Omega \times [0,T]\,, \\ \psi(\mathbf{x},0) = 0 & \mathbf{x} \in \Omega\,, \\ \dfrac{\partial\psi}{\partial t}(\mathbf{x},0) = 0 & \mathbf{x} \in \Omega\,, \\ \text{Boundary condition} & \mathbf{x} \in \Gamma, \end{cases} \tag{1}$$

where the scalar unknown function ψ is either the pressure p or the velocity potential ϕ in the fluid, and $T > 0$ is the considered finite duration. Boundary conditions will be specified in Sec. 3.1.

2.2 | Boundary integral equations for transient acoustic wave propagation problems.

Because Ω is unbounded, it is convenient to reformulate (1) using the boundary integral equation framework. Any field ψ solving (1) admits the integral representation[4]

$$\psi(\mathbf{y},t) = \mathcal{H}\{\psi\}(\mathbf{y},t) - \mathcal{G}\Big\{ \frac{\partial\psi}{\partial n} \Big\}(\mathbf{y},t) \qquad \mathbf{y} \in \Omega,\ t \in [0,T] \tag{2}$$

in terms of its Dirichlet and Neumann traces on Γ, where $\mathcal{G}\{f\}$ and $\mathcal{H}\{g\}$ are the single-layer and double-layer retarded potentials with densities f, g, defined for $\mathbf{y} \in \Omega$ by

$$\mathcal{G}\{f\}(\mathbf{y},t) = \int_\Gamma G(\mathbf{x}-\mathbf{y},t) \star f(\mathbf{x},t)\, \mathrm{d}\Gamma_{\mathbf{x}}, \qquad \mathcal{H}\{g\}(\mathbf{y},t) = \int_\Gamma \frac{\partial G}{\partial n}(\mathbf{x}-\mathbf{y},t) \star g(\mathbf{x},t)\, \mathrm{d}\Gamma_{\mathbf{x}}. \tag{3}$$

In the above definitions, $\star$ denotes the convolution in time and G is the *free space fundamental solution*, given by

$$G(\mathbf{x}-\mathbf{y},t) = \frac{1}{4\pi r}\delta(t - r/c)\,, \qquad r := \|\mathbf{x}-\mathbf{y}\|. \tag{4}$$

On taking the limit as $\mathbf{y} \to \Gamma$ in (2) and invoking well-known results on the limiting values of potentials, any solution to (1) satisfies the boundary integral equation

$$\tfrac{1}{2}\psi(\mathbf{y},t) - \mathcal{H}\{\psi\}(\mathbf{y},t) + \mathcal{G}\Big\{ \frac{\partial\psi}{\partial n} \Big\}(\mathbf{y},t) = 0 \qquad \mathbf{y} \in \Gamma,\ t \in [0,T], \tag{5}$$

where $\mathcal{G}$ and $\mathcal{H}$ are the (weakly singular) boundary integral operators defined by formulas (3) with $\mathbf{y} \in \Gamma$. Substituting the relevant boundary condition into (5) finally produces a BIE governing the remaining unknown, see examples in Sec. 3.1.

2.3 | $\mathcal{Z}$-transform of a causal time convolution.

CQM-based approaches work by reformulating the time-domain BIE (5) in terms of BIEs in the (complex) frequency domain. It can conveniently be presented by focusing on the evaluation of the single-layer integral operator $G\{f\}$ for a given causal density f. This task in turn rests on the evaluation of time convolutions of the form

$$q(t) := (G \star f)(t) = \int_0^t G(t-\tau) f(\tau)\, \mathrm{d}\tau = \int_0^t f(t-\tau) G(\tau)\, \mathrm{d}\tau = (f \star G)(t)\,, \quad \forall t \geq 0\,. \tag{6}$$

The quantity $G(t-\tau)$ may be expressed by inverting the Laplace transform $\bar{G}$ of G (assuming $\bar{G}$ to be well-defined, see Sec. 2.4 for details), so that

$$q(t) = \int_0^t \left(\frac{1}{2\pi i} \int_{\gamma - i\cdot\infty}^{\gamma + i\cdot\infty} \bar{G}(s) e^{s(t-\tau)}\, \mathrm{d}s \right) f(\tau)\, \mathrm{d}\tau\,. \tag{7}$$

Assuming applicability of Fubini's theorem, we obtain

$$q(t) = \frac{1}{2\pi i} \int_{\gamma - i\cdot\infty}^{\gamma + i\cdot\infty} \bar{G}(s) h(t;s) \mathrm{d}s, \qquad \text{with } \; h(t;s) := \int_0^t e^{s(t-\tau)} f(\tau)\, \mathrm{d}\tau\,. \tag{8}$$

Considering a sequence of discrete time instants $t_n = n\Delta t\,, n \in \mathbb{N}$, where Δt is the constant time step, the CQM is developed as a means to evaluate the sequence $(q_n)_{n\geq 0}$ of convolution values $q_n := q(t_n)$, over a finite discrete time interval $\{0, \Delta t, 2\Delta t, \dots, T = M\Delta t\}$, given the sequence $(f_n) := \big(f(t_n)\big)_{n\geq 0}$ and the function G. The key departure point of the CQM consists in remarking that the function $t \mapsto h(t;s)$ introduced in (8) satisfies the initial-value problem

$$\begin{cases} \dfrac{\mathrm{d}h}{\mathrm{d}t}(t;s) = s\, h(t;s) + f(t)\,, \\ h(t \leq 0; s) = 0\,. \end{cases} \tag{9}$$

The ordinary differential equation (9) is numerically solved for the time-discrete approximation $h_n(s) := h(t_n, s)$ of $h(t;s)$ (with fixed s). By applying a linear k-step method (such as the backward Euler method) to (9), the sequence $\big(h_n(s)\big)$ solves

$$\begin{cases} \dfrac{\mathrm{d}h_n(s)}{\mathrm{d}t} \simeq \dfrac{1}{\Delta t} \displaystyle\sum_{j=0}^{k} \alpha_j h_{n+j-k}(s) \;\; = \sum_{j=0}^{k} \beta_j (s h_{n+j-k}(s) + f_{n+j-k})\,, & \forall n \in \mathbb{N}\,, \\ h_{-p}(s) = f_{-p} = 0\,, & \forall p \in [\![1, k]\!]\,, \end{cases} \tag{10}$$

where the coefficients α_j and β_j are the constants of the multistep method (for instance, $k = 1$, $\alpha_0 = -1$, $\alpha_1 = 1$, $\beta_0 = 0$, $\beta_1 = 1$ for the backward Euler method). See e.g., [29, Secs. 11.5 and 11.6].

The next step consists in reformulating equations (10), which relate the sequences $\big(h_n(s)\big)$ and (f_n), in terms of the $\mathcal{Z}$-transforms of those sequences. We recall [26] that the $\mathcal{Z}$-transform $\mathcal{Z}[(x_n)](\xi)$ of a discrete-time signal (x_n) is defined by

$$\mathcal{Z} : (x_n) = \{x_0, x_1, \dots\} \mapsto \mathcal{Z}[(x_n)](\xi) = \sum_{n=0}^{\infty} x_n \xi^n \equiv X(\xi)\,, \quad \xi \in \mathbb{C}\,. \tag{11}$$

The above value $X(\xi)$ of the $\mathcal{Z}$-transform is well defined for $|\xi|$ smaller than the radius of convergence ϱ of the above series. Multiplying the first equation of (10) by $\Delta t\, \xi^n$ for some $\xi \in \mathbb{C}$ and summing over n from 0 to ∞, we obtain

$$\left(\sum_{j=0}^{k} \alpha_j\, \xi^{k-j} \right) H(\xi;s) = \Delta t \left(\sum_{j=0}^{k} \beta_j\, \xi^{k-j} \right) (s\, H(\xi;s) + F(\xi))\,, \tag{12}$$

where $\xi \mapsto H(\xi;s)$ and $\xi \mapsto F(\xi)$ are the $\mathcal{Z}$-transforms of the sequences $\big(h_n(s)\big)$ and $\big(f_n\big)$. Letting $p(\xi)$ denote the ratio

$$p(\xi) = \frac{\sum_{j=0}^{k} \alpha_j\, \xi^{k-j}}{\sum_{j=0}^{k} \beta_j\, \xi^{k-j}}\,, \tag{13}$$

we then have

$$H(\xi;s) = (p(\xi)/\Delta t - s)^{-1} F(\xi). \tag{14}$$

The $\mathcal{Z}$-transform $Q(\xi) := \mathcal{Z}[(q_n)](\xi)$ is readily found, from the expression (8) of $q(t)$ evaluated at instants $t = t_n$, to be given by

$$Q(\xi) = \frac{1}{2\pi \mathrm{i}} \int_{\gamma-\mathrm{i}\cdot\infty}^{\gamma+\mathrm{i}\cdot\infty} \bar{G}(s) H(\xi; s)\, \mathrm{d}s. \tag{15}$$

Using (14) and Cauchy's residue theorem, $Q(\xi)$ is finally found to be related to $F(\xi)$ through

$$Q(\xi) = \frac{1}{2\pi i} \int_{\gamma-i\cdot\infty}^{\gamma+i\cdot\infty} \bar{G}(s) \left(\frac{p(\xi)}{\Delta t} - s \right)^{-1} F(\xi)\, \mathrm{d}s = \bar{G}\left(\frac{p(\xi)}{\Delta t} \right) F(\xi)\,. \tag{16}$$

2.4 | Reformulation of the time-domain BIE.

Since potentials and integral operators involve time convolutions of a causal fundamental solution and a causal density, the developments of Sec. 2.3 are directly applicable to the integral equation formulation of the transient scattering problems, with the help of (16) with $\bar{G}$ taken as the Laplace transform of a fundamental solution. Since the latter is a distribution, we first recall a few facts about the Laplace transform in time before proceeding further.

Let $f \in L^1_{loc}(\mathbb{R})$ be a locally integrable function with support in $\mathbb{R}^+$ (i.e., f is causal), and for which there exists a real number ξ_0 such that $e^{-\xi t} f(t) \in L^1(\mathbb{R})$ for any $\xi \geq \xi_0$ (possibly $\xi_0 = -\infty$). The Laplace transform $\mathcal{L}(f)(s)$ of f is then defined for any $s \in \mathbb{C}$, $\mathrm{Re}(s) > \xi_0$ by

$$\mathcal{L}(f)(s) \equiv \bar{f}(s) = \int_0^{+\infty} f(t) e^{-st} \mathrm{d}t\,, \tag{17}$$

where s is the frequency parameter. More generally, for any causal tempered distribution f, the Laplace transform is defined as[17]

$$\mathcal{L}(f)(s) \equiv \bar{f}(s) = \left\langle f, \exp(-s\,\cdot) \right\rangle, \tag{18}$$

where $\left\langle f, \varphi \right\rangle$ denotes the value of the linear functional f applied to the (causal, smooth) test function φ. In particular, the Laplace transform of the fundamental solution $G(\mathbf{r}, t)$ is obtained, using (18), as

$$\bar{G}(\mathbf{r}, t) = \frac{e^{-sr/c}}{4\pi r}, \qquad r := \|\mathbf{r}\|\,. \tag{19}$$

The inverse Laplace transform may be expressed by the Bromwich integral (or Mellin's inverse formula)

$$\mathcal{L}^{-1}\left(\bar{f}\right)(t) = f(t) = \frac{1}{2\pi i} \int_{\gamma-i\cdot\infty}^{\gamma+i\cdot\infty} \bar{f}(s) e^{+st} \mathrm{d}s\,, \quad \forall t \geq 0\,, \tag{20}$$

where γ is a real number such that $\gamma > r$, where r is such that $\bar{f}(s)$ is analytical in the region $\{s |\, \mathrm{Re}(s) > r\}$ and of polynomial growth at the most.

We begin by applying a collocation method for the time variable to the relevant BIE, enforcing its verification at the discrete time instants t_n, and seek the values $\psi_n := \psi(\cdot, t_n)$ of the unknown at the same time instants. The collocation in time translates into setting to zero the $\mathcal{Z}$-transform of the time-discrete BIE residuals. This is done by applying (16) to the $\mathcal{Z}$-transform of (5), and results in the one-parameter family of BIEs

$$\frac{1}{2}\Psi(\mathbf{y}, \xi) - \int_\Gamma \frac{\partial \bar{G}}{\partial n}(\mathbf{x} - \mathbf{y}) \Psi(\mathbf{x}, \xi)\, \mathrm{d}\Gamma_{\mathbf{x}} + \int_\Gamma \bar{G}(\mathbf{x} - \mathbf{y}) \frac{\partial \Psi}{\partial n}(\mathbf{x}, \xi)\, \mathrm{d}\Gamma_{\mathbf{x}} = 0,$$
$$\mathbf{y} \in \Gamma,\ \xi \in \mathbb{C},\ s = p(\xi)/\Delta t, \tag{21}$$

linking the $\mathcal{Z}$-transforms of the Dirichlet and Neumann traces of solutions ψ to the original problem (1).

Remark 1. The integral operators featured in the BIE (21) are the Laplace transforms of the time-domain operators (3), evaluated at values $s = p(\xi)/\Delta t$ of the complex frequency s. The BIE (21) governs the $\mathcal{Z}$-transform (not the Laplace transform) of the boundary unknown associated with the original propagation problem (1).

Remark 2. When a boundary quantity involves a time derivative (such as in the relationship $p = -\rho\dot{\phi}$ between pressure and velocity potential), we use

$$\mathcal{Z}[d(x_n)](\xi) = \frac{D(\xi)}{\Delta t} \mathcal{Z}[(x_n)](\xi) \tag{22}$$

in the $\mathcal{Z}$ domain, where $D(\xi) := \sum_{j=0}^{k} \alpha_j \xi^{k-j}$ is the symbol of the discrete (time) differentiation operator d embedded in the linear k-step method. When $D(\xi) = p(\xi)$, which is the case e.g., for the backward Euler and BDF2 schemes, the above rule coincides with the differentiation rule of the Laplace transform evaluated at $s = p(\xi)/\Delta t$.

Remark 3. CQM-based solution methods for time-domain BIEs may be introduced and presented in several ways. A common approach is to first introduce the CQM [12,13], whereby a convolution $f \star G$ is expressed with a quadrature whose weights depend on $\bar{G}$, then apply it to the boundary integral equation (5), and finally take the $\mathcal{Z}$-transform of the obtained equation [17]. One alternatively can, following [15], discretise in time the wave equation (1) (recast in first-order form) using a multistep scheme; the resulting PDE governing the $\mathcal{Z}$-transform $\Psi(\cdot, \xi)$ features the wave operator in the Laplace domain with $s = p(\xi)/\Delta t$, and can therefore be reformulated as the BIE (21). This derivation of the $\mathcal{Z}$-BEM avoids having to go into details of the CQM (as in e.g. [14]), in particular because we do not explicitly use the arising weights, allowing a concise presentation of the formulation that stays within the BIE framework.

2.5 | Solution synthesis in the time domain.

Considering for example a Neumann problem (for which ψ is unknown and $\partial_n \psi$ prescribed), the time-discrete physical unknowns $\psi(\cdot, t_n)$ are obtained by taking the inverse $\mathcal{Z}$-transform of $\Psi(\cdot, \xi)$, given by

$$\psi(\cdot, t_k) = \frac{1}{2i\pi} \int_C \Psi(\cdot, \xi) \xi^{-k-1} \, d\xi \,, \quad \forall k \in \mathbb{N} \,, \tag{23}$$

where C is a counterclockwise closed path encircling the origin and entirely in the region of convergence of $\Psi(\cdot, \xi)$. The inversion formula (23) uses the fact that $\psi(\cdot, t_k)$ is the k-th coefficient of the power series expansion of $\Psi(\cdot, \xi)$, by applying Cauchy's residue theorem to $\Psi(\cdot, \xi)$. To evaluate (23) in practice, C is taken as the circle of radius ρ and a trapezoidal rule approximation is considered whereby C is discretised by a set of L complex numbers $\xi_p = \rho e^{2i\pi p/L}$. This provides the approximate value

$$\psi(\cdot, t_k) \approx \frac{1}{L} \sum_{p=0}^{L-1} \Psi(\cdot, \xi_p) \xi_p^{-k} \,, \quad \forall k \in [\![0, M]\!] \,, \tag{24}$$

where M is the total number of time steps. The suitable choice of parameters L, ρ is discussed in [13], where it is shown that setting $L = 2M$ and ρ such that $\rho^L = \varepsilon$ is sufficient to achieve $O(\varepsilon)$ accuracy.
Due to the approximation (24), for $\xi = \xi_p = \rho e^{2i\pi p/L}$, the $\mathcal{Z}$-transforms $(X_p) \equiv (X(\xi_p))$, $X(\xi_p) = \sum_{n=0}^{M} x_n \rho^n e^{2i\pi pn/L}$ (resp. the inverse formula) are evaluated by applying the fast Fourier transform (resp. inverse FFT) to the finite sequence $(x_n \rho^n)_{n=0}^{M}$ $\Big($resp. $(X_p \rho^{-p})_{p=0}^{L-1}\Big)$. Thus, evaluating and inverting the $\mathcal{Z}$-transforms both entail a $O(L \log L) = O(M \log M)$ complexity.

The $2M$ $\mathcal{Z}$-transforms $\Psi(\cdot, \xi_p)$ with $\xi = \xi_p$ $(0 \le p \le 2M-1)$ needed in (24) are governed by the BIEs (21) with $s = p(\xi_p)/\Delta t$, knowing the values $\partial_n \Psi(\cdot, \xi_p)$ of the $\mathcal{Z}$-transform $\partial_n \Psi(\cdot, \xi)$ of the Neumann data. A priori, this entails solving the BIE (21) for all values $\xi = \xi_p$ $(0 \le p \le 2M-1)$ of the $\mathcal{Z}$-transform variable. However, it is easy to show using (21) that $\Psi(\cdot, \bar{\xi}) = \overline{\Psi(\cdot, \xi)}$; moreover we have $\xi_{2M-p} = \overline{\xi_p}$, for $1 \le p \le 2M-1$. As a consequence, the evaluation, using (24), of the complete time-discrete solution needs only $M+1$ BIE solutions, instead of the expected $2M$. In the sequel, references to the number of frequency BEM problems solved take into account this symmetry.

Remark 4. For some discrete-time signal $(\psi_n) = \big(\psi(t_n)\big)$, let $\Psi = \mathcal{Z}[(\psi_n)]$ and $\Psi^{(k)} = \mathcal{Z}[(\psi_n^{(k)})]$, respectively, be the $\mathcal{Z}$-transforms of (ψ_n) and its truncated version $(\psi_n^{(k)}) := \big(\psi_0, \dots, \psi_k, 0, \dots\big)$. Then, applying (23) to Ψ or $\Psi^{(k)}$ yields the same value for $\psi(t_k)$. In other words, (23) is consistent with causality, as the evaluation of $\psi(t_k)$ is unaffected by the contributions to $\mathcal{Z}[(\psi_n)]$ of the time-discrete signal at later times.

2.6 | Summary of the computational procedure.

Considering again a Neumann problem for definiteness, the $\mathcal{Z}$-BEM proceeds as follows:

- For each $k \in [\![0, M]\!]$, find $\Psi(\cdot, \xi_k)$ by solving the BIE (21) with $\xi = \xi_k$ and $s = p(\xi_k)/\Delta t$, $\partial_n \Psi(\cdot, \xi_k)$ being given;
- For each $k \in [\![1, M-1]\!]$, set $\Psi(\cdot, \xi_{2M-k}) = \overline{\Psi(\cdot, \bar{\xi}_k)}$;
- Compute each term of the sequence $\psi(t_n)$ by the (approximate) inverse $\mathcal{Z}$-transform (24), wherein $L = 2M$.

Concluding, the $\mathcal{Z}$-BEM allows to solve the time-domain BIE (5) at discrete time instants $t = 0, \Delta t, 2\Delta t, \dots, M\Delta t = T$, by solving $M + 1$ Laplace-domain BIEs, whose input can be computed with $O(M \log M)$ complexity. The overall complexity of the $\mathcal{Z}$-BEM is mainly determined by the $M + 1$ frequency BIEs, to be solved using a fast BEM solver.

2.7 | Fast frequency-domain BEM solvers.

The foregoing $\mathcal{Z}$-BEM procedure crucially relies upon solving BIEs (21) in the (complex) frequency-domain that may involve large BE discretisations. This has the definite advantage of relying on well-established formulations, in particular existing fast BEM solvers for frequency-domain problems. We summarize next the fast BEM framework used in this work.

The BEM is based on the discretisation of boundary integral equations, thus avoiding the discretisation of the entire domain Ω. All available BEM discretisation methods are compatible with the $\mathcal{Z}$-transform framework. We use the collocation method, in which boundary integral equations are enforced at a finite number of points on the surface, called collocation points[30,4]; other possibilities include the Galerkin method[31,32,10,8,33]. Once discretised with the collocation approach, the BIE (21) yields a linear system of the form

$$[\mathbf{H}]\{\boldsymbol{\psi}\} = [\mathbf{G}]\{\mathbf{Q}\}, \tag{25}$$

where the N-vectors $\{\boldsymbol{\psi}\}$ and $\{\mathbf{Q}\}$ are the discretised traces of ψ and $-\partial_n\psi$ on the discretised boundary, and $[\mathbf{G}]$, $[\mathbf{H}]$ are $N \times N$ matrix discretisations of $\mathcal{G}$ and $1/2 - \mathcal{H}$, respectively. Given the boundary conditions of a specific problem, the generic equation (25) is rewritten as:

$$[\mathbf{K}]\{\mathbf{v}\} = \{\mathbf{f}\}, \tag{26}$$

where the $N \times N$ influence matrix $[\mathbf{K}]$ is related to $[\mathbf{G}]$ or $[\mathbf{H}]$, and $\{\mathbf{v}\}$, $\{\mathbf{f}\}$ are N-vectors collecting the DOFs that remain unknown and quantities known from the boundary conditions, respectively. For instance, for a Neumann problem where $\partial_n\psi$ is prescribed on Γ, $[\mathbf{K}] = [\mathbf{H}]$, $\{\mathbf{v}\} = \{\boldsymbol{\psi}\}$ and $\{\mathbf{f}\} = [\mathbf{G}]\{\mathbf{Q}\}$. By contrast with the FEM (see e.g.,[34]), the matrices $[\mathbf{H}]$, $[\mathbf{G}]$ and $[\mathbf{K}]$ are fully populated and (for the collocation approach adopted here) non-symmetric[5,30]. Applying direct solvers to the system (26) entails a $O(N^3)$ complexity, which is unacceptable for large-scale problems. For that reason, (26) is iteratively solved using the Generalised Minimal RESidual method (GMRES)[35]. The major time-consuming task then becomes the evaluation of a matrix-vector product $[\mathbf{K}]\{\mathbf{v}\}$ at each GMRES iteration, with a $O(N^2)$ complexity still unacceptable for large-scale problems.

Fast BEMs act by accelerating each evaluation of $[\mathbf{K}]\{\mathbf{v}\}$ without actually forming the full matrix $[\mathbf{K}]$. Available BEM acceleration methods include the Fast Multipole Method (FMM), which has proved very efficient and flexible for wave propagation problems[36,20,21,37], and hierarchical matrix ($\mathcal{H}$-matrix) based solvers, which use low-rank approximations of recursively defined off-diagonal matrix blocks[38,39]. In this work, the BEM is accelerated using the multi-level FMM, implemented in the in-house FM-BEM solver *COFFEE* (`https://uma.ensta-paris.fr/soft/COFFEE/`). The computational complexity of each matrix-vector product is then $O(N \log N)$, instead of $O(N^2)$. We provide for completeness an overview of the FM-BEM in A, and refer to[36] for implementation details.

3 | IMPROVEMENTS OF THE PROCEDURE FOR RAPID TRANSIENT PROBLEMS

The $\mathcal{Z}$-BEM procedure presented in Sec. 2 still lacks efficiency when dealing with rapid transient problems involving large numbers of small time steps, even in FMM-accelerated form, because it entails solving BIEs (21) for a large number of high complex frequencies ($s(\xi) = p(\xi)/\Delta t$ becoming large for small time steps). In Secs. 3.2 to 3.6, we present proposed improvements to the $\mathcal{Z}$-BEM procedure that specifically address this concern and are applicable to all rapid transient problems, such as those arising in our target FSI analyses. To this end, we first motivate and summarize the two types of wave propagation problems addressed, namely radiation and scattering problems (see Sec. 3.1).

3.1 | Radiation and scattering problems for FSI applications.

This work is motivated by eventual applications to FSI problems, which involve a deformable structure (or a set thereof) occupying the bounded region Ω_s and facing incoming waves in the surrounding acoustic fluid. In this context, it is convenient to decompose the total pressure field p^{tot} in Ω into a sum of three components: $p^{\text{tot}} = p^{\text{inc}} + p^{\text{ref}} + p^{\text{rad}}$[40]. The incident field p^{inc} defines the acoustic field in the absence of the structure. The reflected field p^{ref} is the pressure perturbation that would arise were the structure motionless. The radiated field p^{rad} is then the correction to the fluid state due to the motion of the structure, which radiates an acoustic wave into the fluid (Fig. 2). This leads us to focus in this work on the cases of (i) wave scattering

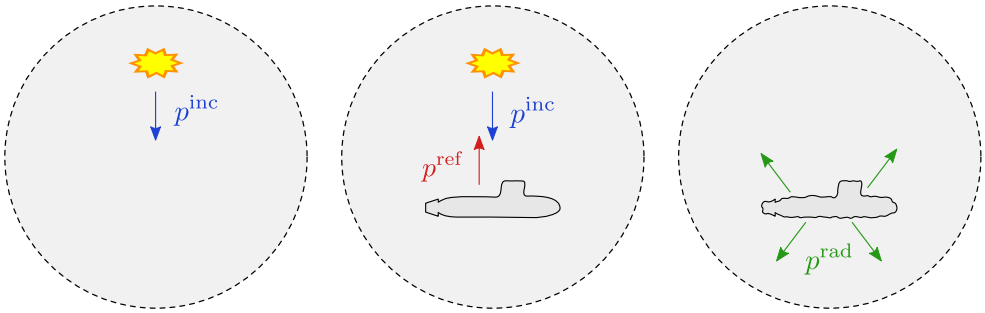

FIGURE 2 Decomposition of the fluid variables into incident, reflected and radiated parts.

by a motionless geometry, and (ii) radiation of a wave by a given structure motion. Both cases are formulated by invoking the kinematic boundary condition $\boldsymbol{\nabla}\phi\cdot\mathbf{n} = \mathbf{v}\cdot\mathbf{n} =: u$ on Γ (where $\nabla\phi$ and $\mathbf{v}$ are respectively the fluid and solid velocities on Γ). The respective pressure fields p^{ref} and p^{rad} thus solve (1) together with the Neumann boundary condition

$$\begin{aligned} \partial_n p^{\text{rad}} &= -\rho\,\dot{u} && \text{case (i)},\\ \partial_n p^{\text{ref}} &= -\partial_n p^{\text{inc}} && \text{case (ii)}. \end{aligned} \tag{27}$$

Substituting these in (5) and using the notations of Sec. 2, the radiated pressure field p^{rad} for case (i) solves the boundary integral equation

$$\tfrac{1}{2}p^{\text{rad}}(\mathbf{y},t) - \mathcal{H}\{p^{\text{rad}}\}(\mathbf{y},t) = \mathcal{G}\big\{\rho\dot{u}\big\}(\mathbf{y},t) \qquad \mathbf{y}\in\Gamma,\ t\in[0,T]. \tag{28}$$

Similarly, the total pressure $p^{\text{Ref}} := p^{\text{inc}} + p^{\text{ref}}$ for case (ii) satisfies the BIE

$$\tfrac{1}{2}p^{\text{Ref}}(\mathbf{y},t) - \mathcal{H}\{p^{\text{Ref}}\}(\mathbf{y},t) = p^{\text{inc}}(\mathbf{y},t) \qquad \mathbf{y}\in\Gamma,\ t\in[0,T], \tag{29}$$

where we took advantage of the fact that the incident field p^{inc} satisfies the interior BIE

$$\tfrac{1}{2}p^{\text{inc}}(\mathbf{y},t) + \mathcal{H}\{p^{\text{inc}}\}(\mathbf{y},t) - \mathcal{G}\{\partial_n p^{\text{inc}}\}(\mathbf{y},t) = 0 \qquad \mathbf{y}\in\Gamma,\ t\in[0,T]. \tag{30}$$

The respective discretised BEM systems for the $\mathcal{Z}$-transforms of the total field $\mathbf{P}^{\text{Ref}}$ in the reflected case or $\mathbf{P}^{\text{rad}}$ in the radiation case therefore have the form

$$\left.\begin{aligned} \mathbf{H}(s)\{\mathbf{P}^{\text{rad}}(\xi)\} &= s\rho\,\mathbf{G}(s)\{\mathbf{U}(\xi)\} && \text{case (i)}\\ \mathbf{H}(s)\{\mathbf{P}^{\text{Ref}}(\xi)\} &= \mathbf{P}^{\text{inc}}(\xi) && \text{case (ii)} \end{aligned}\right\} \qquad s = p(\xi)/\Delta t\,. \tag{31}$$

Remark 5. Although we focus in this work on exterior Neumann problems, the methods proposed are easily transposable to other types of exterior boundary-value problems (e.g., involving Dirichlet or Robin boundary conditions).

3.2 | Reducing the number of BEM problems through a high-frequency approximation.

Using small time steps Δt in either BEM system (31) means that most of the complex frequencies $s(\xi)$ are high. It is therefore useful to exploit any available results pertaining to high-frequency approximations of dynamical problems. For deformable solids, the high-frequency range is defined as *the frequency band for which there is a uniform high modal density*[41]. For wave scattering problems, a frequency may be considered as high if the ratio κ/λ between the local radius of curvature κ and the characteristic wavelength λ is large.

Here, we propose to improve our $\mathcal{Z}$-BEM treatment by relying on the assumed availability of an asymptotic high-frequency approximation (HFA) of solutions to (21) which can be invoked whenever $|s(\xi_k)| = |p(\xi_k)|/\Delta t > f_{\text{HFA}}$ for some threshold frequency f_{HFA}. Then, BEM problems (25) are actually solved when $|s(\xi_k)| \le f_{\text{HFA}}$ whereas a (faster to evaluate) HFA approximation is used instead when $|s(\xi_k)| > f_{\text{HFA}}$. The main issue then is whether and how a HFA and a threshold f_{HFA} can be satisfactorily defined. For the present study (and its intended applications), the answer differs according to whether a radiation or a scattering problem is being solved.

3.3 | HFA for wave radiation problems.

We first consider the case of waves radiated into a fluid by a moving structure (case (i) in (27)). For such problems, a simple HFA consists in setting $p \approx \rho c u$. The physical interpretation of this HFA lies in the fact that, if the surface Γ is smooth and vibrates

at a high frequency, the radiated pressure at $\mathbf{y} \in \Gamma$ is determined by interactions with points close to $\mathbf{y}$ (due to causality), which approximately lie on the tangent plane to Γ at $\mathbf{y}$. Then, the radiated pressure resembles that of a vibrating infinite plate, which is known to be given by $p = \rho c u$. In this case, where an explicit HFA is available, the procedure relies on the evaluation of relative differences

$$\delta_{\mathrm{HFA}}(s) := \frac{\|\psi_{\mathrm{BEM}}(s) - \psi_{\mathrm{HFA}}(s)\|_{L^2(\Gamma)}}{\|\psi_{\mathrm{BEM}}(s)\|_{L^2(\Gamma)}}, \tag{32}$$

and the choice of a preset tolerance tol. The steps are then the following:

- Solve BEM problems (25) for frequencies $s(\xi_k) = p(\xi_k)/\Delta t$ of increasing modulus;
- After each solution, compare the BEM and HFA solutions, for instance in terms of δ_{HFA};
- Set the cut-off frequency f_{HFA} to that value of $|s(\xi_k)|$ for which $\delta_{\mathrm{HFA}} \leq \mathrm{tol}$;
- Use the HFA to approximate the solution of all BEM problems with $|s(\xi_k)| > f_{\mathrm{HFA}}$ (i.e., do not solve (25) in those cases).

The efficiency of the procedure relies on the number M_B of frequency-domain BEMs to be actually solved, which depends on several parameters, such as the tolerance tol, but more importantly on the high-frequency nature of the considered problem. This approach is exemplified in Sec. 4.1, where numerical results are presented in the simple case of a breathing sphere.

3.4 | HFA for wave scattering problems.

The foregoing approach may be applied whenever an explicit HFA is known. This is not the case for scattering problems (case (ii) in (27)), for which in particular f_{HFA} can no longer simply be set against a preset tolerance. We propose instead an ad hoc treatment.

The starting point for finding approximate solutions to this class of problems is the Kirchhoff HFA[42]. This idea is also used in the high-frequency BEM literature[43,44,45] Let $\mathbf{s} \in \Omega$ denote a source point emitting spherical waves. Then, $\mathbf{d}(\mathbf{y}) := (\mathbf{y} - \mathbf{s})/\|\mathbf{y} - \mathbf{s}\|$ is the propagation direction of the incident wave at $\mathbf{y} \in \Gamma$. The Kirchhoff HFA for the total pressure p^{ref} on Γ is ($p^{\mathrm{Ref}} \equiv p$)

$$p_{\mathrm{HFA}}(\mathbf{y}, t) = 0 \qquad \text{if } \mathbf{d}(\mathbf{y}) \cdot \mathbf{n}(\mathbf{y}) > 0; \qquad p_{\mathrm{HFA}}(\mathbf{y}, t) = 2p^{\mathrm{inc}}(\mathbf{y}, t) \qquad \text{if } \mathbf{d}(\mathbf{y}) \cdot \mathbf{n}(\mathbf{y}) < 0. \tag{33}$$

This simple HFA is known to provide accurate results in the regions of Γ where $|\mathbf{d}(\mathbf{y}) \cdot \mathbf{n}(\mathbf{y})| \simeq 1$. On the other hand, in the region where $|\mathbf{d}(\mathbf{y}) \cdot \mathbf{n}(\mathbf{y})| \simeq 0$, this HFA is discontinuous and hence imprecise.

Our purpose is to heuristically define an improved approximation of the same type, ensuring a similarly low computation time. The idea is to find a coefficient $C = C(\mathbf{y})$, depending on the evaluation point $\mathbf{y} \in \Gamma$, relating the $\mathcal{Z}$-transforms through $P_{\mathrm{HFA}} = C(\mathbf{y}) P^{\mathrm{inc}}$.

To describe our HFA, we study a HF example problem involving a long cylinder facing a spherical wave (see details in Sec. 4.2, see Fig. 5). BEM problems (25) are solved for complex frequencies s of increasing modulus. For a point $\mathbf{y} \in \Gamma$, we introduce the complex ratio

$$\mathcal{R}(\mathbf{y}, s) \equiv P(\mathbf{y}, s)/P^{\mathrm{inc}}(\mathbf{y}, s)\,. \tag{34}$$

If the obstacle is convex, it can be shown[43,44,45] that for any point $\mathbf{y} \in \Gamma$, $s \mapsto \mathcal{R}(\mathbf{y}, s)$ becomes approximately constant (with $\mathrm{Im}\,\mathcal{R}$ small relative to $\mathrm{Re}\,\mathcal{R}$) as $|s|$ becomes large (see Fig. 7). On the basis of these observations, we propose the following, empirical, HFA construction:

- Choose a cut-off frequency f_{HFA} until which all problems (25) are solved; f_{HFA} then is the highest frequency modulus for which the BIE (21) is solved using the $\mathcal{Z}$-BEM procedure;
- Assume $\mathcal{R}(\mathbf{y}, s)$ to remain constant for $|s| > f_{\mathrm{HFA}}$, and define the HFA approximation of $P(\cdot, s)$ for any $|s| > f_{\mathrm{HFA}}$ by $P_{\mathrm{HFA}}(\mathbf{y}, s) = \mathcal{R}(\mathbf{y}) P^{\mathrm{inc}}(\mathbf{y}, s)$, with $\mathcal{R}(\mathbf{y}) := \mathcal{R}(\mathbf{y}, f_{\mathrm{HFA}})$.

Of course, the numerical gain lies in approximating the solution of a given frequency-domain scattering problem by means of a simple multiplication, instead of solving a costly BEM problem. The required number of BEM solutions in this framework depends on the high-frequency nature of the original problem (see Sec. 4). We also tried the HFA variant $P_{\mathrm{HFA}}(\mathbf{y}, s) = \mathrm{Re}(\mathcal{R}(\mathbf{y})) P^{\mathrm{inc}}(\mathbf{y}, s)$, which produced similar results.

The best value of f_{HFA} is impossible to determine *a priori*. In practice, one may choose between two alternatives: (a) set f_{HFA} to the highest possible value for which the BEM problem can practically be solved for given computer resources (given that increasing $|s|$ entails refining the BE mesh), or (b) set an arbitrary initial guess for f_{HFA}, then gradually increase its value until the results in the time domain are deemed satisfactory (the errors induced by a too-low value of f_{HFA} are easily recognisable). Numerical experiments for this approach will be discussed in Secs. 4.2 and 4.3.

3.5 | HFA yields $O(1)$ complexity in time.

The spatial complexity of the FM-BEM is $O(N \log N)$. Asymptotically, the time complexity of our procedure is given by the complexity of the $\mathcal{Z}$-transform, computed with an FFT, so $O(M \log M)$. However, performing the FFT is much faster than solving a BEM problem. Then, in practice, for reasonable values of M (we tried up to $M = 10^5$), the time complexity of the procedure depends on the number M_B of frequency-domain BEM problems actually solved. Without recourse to a HFA, we have $M_B = M + 1$, see Sec. 2.6. By contrast, the availability of a HFA, such that BEM problems are solved only when $|p(\xi)|/\Delta t \le f_{\mathrm{HFA}}$ for some threshold f_{HFA}, has the remarkable consequence of making the overall complexity in time constant (instead of linear). More precisely:

Proposition 1. Assume that all zeros of $p(\xi)$, except $\xi = 1$, have modulus strictly greater than 1. Let $\xi_k = \rho e^{\mathrm{i}k\pi/M}$ $(0 \le k \le 2M-1)$ with ρ such that $\rho^M = \varepsilon$, in accordance with the synthesis formula (24) used for discrete times $t_n = n\Delta t$ $(0 \le n \le M)$. Let $M_0 \in \mathbb{N}$. For a given threshold f_{HFA} and any $M \ge M_0$, there exists $K \in \mathbb{N}$ depending only on f_{HFA}, M_0 and the chosen multistep method (in particular, K does not depend on Δt) such that we have

$$\frac{|p(\xi_k)|}{\Delta t} \ge f_{\mathrm{HFA}} \qquad \text{for all} \quad k \in [\![K, 2M-K]\!].$$

In other words, for any large enough M, the number of complex frequencies with modulus smaller than a chosen HFA threshold is at most $2K-1$.

Proof. Let B denote the closed unit disk in the complex plane. We begin by observing that the consistency requirement for the linear multistep method dictates that $\xi = 1$ be a single root of the symbol $p(\xi)$[29, Secs. 11.5 and 11.6]; we can then write $p(\xi) = (1-\xi)q(\xi)$, with $q(1) \ne 0$. Having assumed that all other zeros of p have modulus strictly greater than 1, there exists $q_0 > 0$ such that $|q(\xi)| \ge q_0$ for all $\xi \in B$, and we have $|p(\xi)| \ge q_0|1-\xi|$.

Then, for the values $\xi_k = \rho e^{\mathrm{i}k\pi/M}$ $(0 \le k \le 2M-1)$ of interest, we have

$$|1-\xi_k|^2 = (1-\rho)^2 + 2\rho\big(1 - \cos\big((k\pi/M)\big)\big). \tag{35}$$

Moreover, letting ρ_0 be defined by $\rho_0^{M_0} = \varepsilon$, we have $1 \ge \rho \ge \rho_0$ for any $M \ge M_0$.

Case 1: $\cos(k\pi/M) \ge 0$.

For this case, observing in addition that $(1-\rho)^2 \ge 0$ and $1 - \cos u \ge (4/\pi^2)u^2$ for any $u \in [-\pi/2, \pi/2]$, we get

$$|p(\xi_k)|^2 \ge q_0^2|1-\xi_k|^2 \ge \frac{8}{\pi^2} q_0^2 \rho_0 \Big(\frac{k\pi}{M}\Big)^2.$$

This implies that

$$\frac{|p(\xi_k)|^2}{\Delta t^2} = \frac{M^2|p(\xi_k)|^2}{T^2} \ge f_{\mathrm{HFA}}^2 \qquad \text{for any } \ k,\ K \le |k| \le \frac{M}{2}, \qquad \text{with } \ K := \Big\lfloor \frac{f_{\mathrm{HFA}}T}{q_0\sqrt{8\rho_0}} \Big\rfloor,$$

where $\lfloor x \rfloor$ denotes the integral part of $x \in \mathbb{R}$. Consequently, the inequality $|p(\xi)|/\Delta t \le f_{\mathrm{HFA}}$ of main interest can possibly be verified only by $\xi = \xi_k$ with $1-K \le k \le K-1$, i.e., has at most $2K-1$ solutions such that $\cos(k\pi/M) \ge 0$.

Case 2: $\cos(k\pi/M) \le 0$.

In that case, (35) implies that $|p(\xi)|^2 \ge 2\rho_0 q_0^2$, while $\Delta t \le T/M_0$, so the target inequality $|p(\xi)|/\Delta t \le f_{\mathrm{HFA}}$ implies

$$q_0 M_0 \sqrt{2\rho_0} = \sqrt{2} q_0 M_0 \varepsilon^{1/2M_0} \le f_{\mathrm{HFA}} T,$$

with the equality resulting from the definition of ρ_0. Since $M_0\varepsilon^{1/2M_0} \to \infty$ as $M_0 \to \infty$, M_0 can be selected such that

$$q_0 M_0 \sqrt{2\rho_0} \ge f_{\mathrm{HFA}} T$$

in which case any ξ_k such that $\cos(k\pi/M) \le 0$ violates the target inequality $|p(\xi)|/\Delta t \le f_{\mathrm{HFA}}$.
On combining the outcomes of cases 1 and 2, the proof is complete. □

Proposition 1 and its proof mean that, after taking advantage of both the HFA and the symmetry under conjugation of ξ_k mentioned in Sec. 2.5, the expected number of actually required BEM solutions satisfies the estimate

$$M_B \le 1 + \Big\lfloor \frac{f_{\mathrm{HFA}}T}{q_0\sqrt{8\rho_0}} \Big\rfloor, \tag{36}$$

which depends only very mildly in M_0 (we have e.g., $\sqrt{\rho_0} \approx 0.75, 0.97, 0.997$ for $M_0 = 10, 100, 1000$).

Remark 6. The assumption made on the zeros of $p(\xi)$ in Prop 1, which is verified e.g., by the backward Euler and BDF2 schemes, is equivalent to assuming that all zeros of the characteristic polynomial of the numerical differentiation operator underlying the multistep scheme, except $\xi = 1$, lie outside the closed unit disk of $\mathbb{C}$, i.e., that the multistep scheme is *strongly stable* (see e.g., [29, Secs. 11.5 and 11.6] for an overview of the properties of multistep methods).

For multistep schemes that are only *zero-stable*, $p(\xi)$ has other zeros (of multiplicity 1) on the unit circle, which would provide additional clusters of points ξ_k satisfying $|p(\xi_k)|/\Delta t \leq f_{\text{HFA}}$.

3.6 | Adapting the mesh refinement to the complex frequency.

For a given wave propagation problem, the BEM problems (25) are solved with a fast FM-BEM solver. This solver is efficient with a fixed number of nodes per wavelength (typically 10 or so)[36]. This implies that using the same mesh for all frequencies is not efficient. On the other hand, generating a mesh for each frequency is impractical. To strike a balance, about 10 meshes of Γ are created, with uniform and decreasing mesh size. For a given frequency $s(\xi_k)$, the associated BEM problem is solved using the least refined mesh that has at least 8 points per wavelength, and the BEM solutions obtained on that mesh are interpolated to a master mesh (chosen for post-processing, or in the future for fluid-structure coupling) using the software feflo.a[46].

4 | NUMERICAL VALIDATION

In view of the industrial context of our study, we choose to validate the fast $\mathcal{Z}$-BEM method described in Secs. 2 and 3 on simple configurations that are representative of the interaction between an underwater explosion and a submarine. The resulting blast is a spherical wave that propagates in an unbounded acoustic medium at speed c, before interacting with a shell whose surface is known. Two academic problems are accordingly considered in this section to demonstrate the efficiency of the $\mathcal{Z}$-BEM: a breathing sphere, and the scattering of a spherical wave by a rigid infinite cylinder. Reference solutions are available for both problems, see B and C. Results on a more-complex configuration evocative of the industrial problem will then be presented in Sec. 5.

All numerical results of this section have been obtained under the following conditions:

- The accuracy ϵ of the discrete inverse $\mathcal{Z}$-transform (24) is set to 10^{-5};
- The number of frequencies L is set to twice the number of time steps: $L = 2M$;
- The value of ρ is set according to ϵ, such that $\rho^L = \epsilon$;
- The backward differentiation formula of order 2 (BDF2) is used: $p(\xi) = (3 - 4\xi + \xi^2)/2$;
- The GMRES tolerance for the FM-BEM frequency-domain solver is set to 10^{-5};
- The fluid velocity and mass density are $c = 1500\,\text{m/s}$ and $\rho = 1000\,\text{kg/m}^3$, respectively.

The two possible sources of errors when using the $\mathcal{Z}$-BEM procedure are (i) the FM-BEM procedure, and (ii) the CQM-HFA procedure. The FM-BEM procedure used here has already been validated[36,47], both in terms of convergence and complexity of the method. We will thereafter evaluate solution errors against a reference solution p_{ex}, which reflect the cumulative effect of sources (i) and (ii), expecting factor (ii) to be dominant.

4.1 | First validation case: breathing sphere.

Consider a spherical shell of radius a, submerged in an infinite fluid domain Ω, with mass density ρ and sound velocity c. The shell and fluid are both at initial rest. At time $t = 0$, the shell starts pulsating, or breathing, with a radially-symmetric normal velocity $u = \mathbf{u} \cdot \mathbf{n}$; this creates a radiated field in the surrounding fluid. We look for the induced acoustic pressure in the fluid domain, and more specifically on the sphere surface $\Gamma = \{r = a\}$. This radiation problem consists in solving (1) for $\psi = \phi$ with the boundary condition

$$\partial_n \phi(\mathbf{y}, t) = u(t), \quad \mathbf{y} \in \Gamma = \{r = a\}, \tag{37}$$

expressing the prescribed normal wall velocity u. The results presented in this section are obtained with u set to

$$u(t) = u(t; \omega) = u_0 \sum_{i=1}^{5} u_i \sin(2\pi f_i t), \tag{38}$$

where $u_1 = 1$, $u_2 = 1.2$, $u_3 = 0.7$, $u_4 = 2.8$, $u_5 = 1.4$, and the frequencies are set to $f_1 \equiv 2\pi\omega = f_{\max}$, $f_2 = f_{\max}/1.7$, $f_3 = f_{\max}/2.4$, $f_4 = f_{\max}/7.6$, $f_5 = f_{\max}/25.4$. The angular frequency parameter ω is fixed[1]. The amplitude u_0 is assumed to be small enough for the linear acoustic fluid model to be correct. This problem has a closed-form analytical solution p_{ex}, see B.

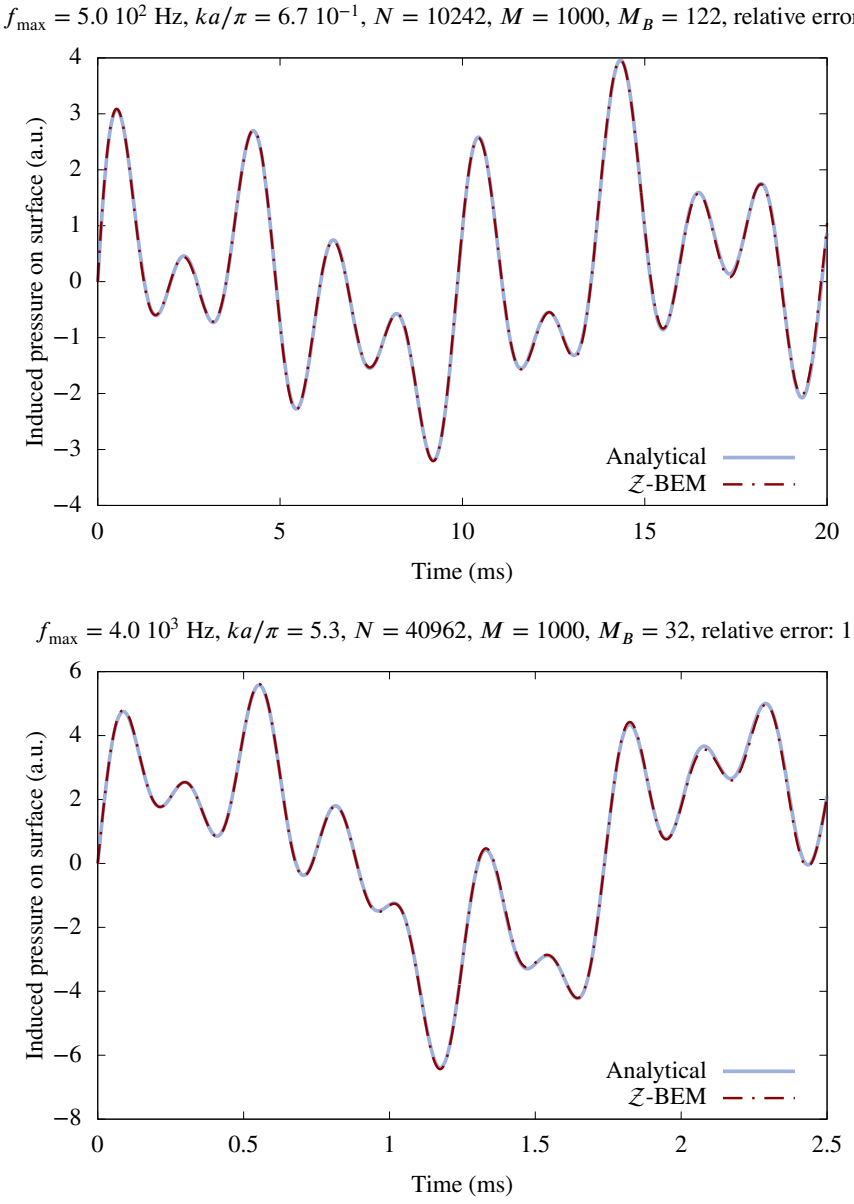

FIGURE 3 Breathing sphere: pressure induced on the surface (with $k = \omega/c$).

Figure 3 shows that the pressure p^{rad} on Γ computed using our fast $\mathcal{Z}$-BEM procedure agrees very well with the analytical solution p_{ex}, with relative errors (see (39)) $\delta(\Gamma) = 1.3\%$ and $\delta(\Gamma) = 1.7\%$ for the two considered values $f_{\max} = 5\ 10^2$ Hz and $f_{\max} = 4\ 10^3$ Hz of the prescribed frequency. The latter are typical of situations where a submarine faces a remote underwater explosion, where T is of the order of a few milliseconds.

We now examine the influence of the HFA ($\boldsymbol{P}^{\text{rad}} = \rho c \boldsymbol{U}$ in this case, see Sec. 3.3) on both solution accuracy and computational efficiency. The BEM problems are solved for the requisite frequencies $s(\xi_k) = p(\xi_k)/\Delta t$, taken in order of increasing modulus. Each BEM solution is compared to its HFA approximation by way of the relative difference δ_{HFA} (see (32)), with $\delta_{\text{HFA}}(s(\xi_k))$

[1]This is **not** a time-harmonic problem, since the sphere **starts** breathing at $t = 0$, a time-harmonic steady state being reached only in the infinite-time limit.

expected to decrease as $|s(\xi_k)|$ increases. For a certain frequency $s = s_{\mathrm{HF}}$, $\delta_{\mathrm{HFA}}(s)$ becomes smaller than a preset tolerance $\mathrm{tol}_{\mathrm{HFA}}$ (typically 5 %). Then, the high-frequency limit f_{HFA} is set to $|s_{\mathrm{HF}}|$, and BEM solutions for $|s(\xi_k)| > f_{\mathrm{HFA}}$ are evaluated using the HFA.

TABLE 1 Breathing sphere: influence of the choice of f_{HFA} on time-domain solution accuracy (with $k_{\mathrm{HFA}} = 2\pi f_{\mathrm{HFA}}/c$). Relative difference indicators δ_{HFA} and $\delta(\Gamma)$ are defined by (32) and (39).

$f_{\mathbf{max}}$ **(kHz)**	$f_{\mathbf{HFA}}$ **(kHz)**	$k_{\mathbf{HFA}}a/\pi$	M_B	$\delta_{\mathbf{HFA}}(f_{\mathbf{HFA}})$ **(%)**	$\delta(\Gamma)$ **(%)**
(a) 0.5	6.6	8.9	43	22.2	4.7
	8.0	10.6	51	19.5	3.2
	9.9	13.3	63	12.9	2.1
	13.3	17.7	83	12.5	1.9
	19.9	26.6	122	6.5	1.7
	39.8	53.1	224	3.6	1.7
(b) 4.0	17.7	23.6	15	8.4	4.6
	26.6	35.4	22	5.8	4.1
	39.8	53.1	32	3.7	1.3
	79.7	106.3	63	1.9	1.2

Table 1 illustrates the influence of f_{HFA} on the accuracy of the transient solution, employing the two previously considered values of $f_{\max}$ in (38). It also shows the corresponding number M_B of frequency-domain BEM solutions computed, the relative BEM-HFA difference δ_{HFA} at frequency f_{HFA} (see (32)) and the overall solution error

$$\delta(\Gamma) := \frac{\|p - p_{\mathrm{ex}}\|_{L^2([0,T];L^2(\Gamma))}}{\|p_{\mathrm{ex}}\|_{L^2([0,T];L^2(\Gamma))}}. \tag{39}$$

As expected, $\delta(\Gamma)$ decreases when f_{HFA} is increased, while the overall solution error steadily reduces until reaching a limiting value that is the best accuracy achievable with the considered mesh. Therefore, the procedure appears to be both consistent and accurate.

The fast $\mathcal{Z}$-BEM procedure is seen to accurately solve rapid acoustic radiation problems in the time domain at the cost of only a moderate number M_B of frequency BEM solutions, thanks to a HFA. The gain of the method lies in the number of frequency BEM problems solved: as shown in Proposition 1, M_B for a given physical problem is asymptotically independent of the time step Δt. Indeed, selecting an overly small time step should not artificially increase the number of BEM problems, as this does not *per se* mean that the considered physical problem is a high frequency one. On the other hand, M_B decreases as the intrinsic high-frequency character of the problem increases, as more information on the solution is then provided by the HFA. Case (b) of Table 1 clearly illustrates the efficiency of the procedure: only $M_B = 32$ BEM solutions are needed (the $M + 1 - M_B = 969$ missing frequency-domain solutions being provided by the HFA) to achieve an accuracy of 1.3%, that is nearly the same as that obtained without HFA (at the cost of $M + 1 = 1001$ BEM solutions). Moreover, these M_B solutions can be computed concurrently (see Sec. 5.1). Going to the other extreme of solving case (b) using only the HFA (no BEM solution), the obtained solution is expected to be accurate only for the first time steps, and this is corroborated by Fig. 4. The best compromise between accuracy and efficiency then clearly has to combine BEM and HFA solutions.

4.2 | Second validation case: rigid infinite cylinder facing a spherical wave.

We now consider the scattering of a wave by an infinite cylinder, a configuration more representative of our intended applications, which allows comparisons to a semi-analytical reference solution. The incident wave results from the explosion of $W = 100\,\mathrm{kg}$ of TNT at a point $\mathbf{s}$ whose distance to the cylinder axis is $d_0 = 100\,\mathrm{m}$ (see Fig. 5). It is an abrupt acoustic wave whose pressure field is empirically expressed as [1]

$$p^{\mathrm{inc}}(\mathbf{y}, t) = p_m(r) \exp\left(-\frac{t - r/c}{\tau(r)}\right) H(t - r/c), \qquad r = \|\mathbf{y} - \mathbf{s}\|, \tag{40}$$

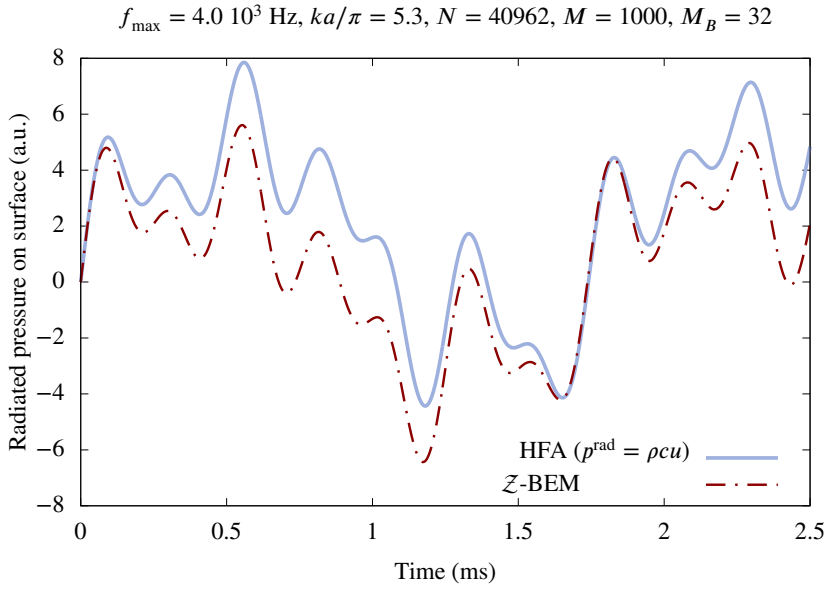

FIGURE 4 Breathing sphere: $\mathcal{Z}$-BEM solution and HFA for the radiated pressure p^{rad} on Γ.

where

- H is the Heaviside step function,
- $p_m(r) = K_1 \left(\frac{W^{1/3}}{r}\right)^{a_1}$ is the magnitude of the initial pressure jump,
- $\tau(r) = K_2 W^{1/3} \left(\frac{W^{1/3}}{r}\right)^{a_2}$ characterises the pressure decay in time.

K_1, K_2, a_1, a_2 are parameters that depend on the kind of explosive material; the values

$$K_1 = 5.24\ 10^7 \text{ SI},\ a_1 = 1.13, \qquad K_2 = 8.4\ 10^5 \text{ SI},\ a_2 = -0.23.$$

were used to obtain the results presented thereafter[48]. A sum of two exponentials[49] could equally well be considered in (40) without affecting our procedure, which is independent of the form of the input pressure (as long as it is a HF sollicitation). Numerical results yielded by our fast $\mathcal{Z}$-BEM, incorporating all improvements presented in Sec. 3, are compared to those provided by an in-house implementation of the semi-analytical approach given in C. The $\mathcal{Z}$-BEM procedure is in particular used with the mesh interpolation presented in Sec. 3.6, carried out with 8 meshes with uniform decreasing mesh size. For the $\mathcal{Z}$-BEM computations, a finite cylinder is considered, axially long enough to ensure that the results obtained for the considered duration T coincide (due to causality) to those for an infinite cylinder. The following parameters were used for the $\mathcal{Z}$-BEM computations: $T = 5$ ms (with results only shown for $T = 3$ ms to ensure their insensitivity to the finite cylinder length), $f_{\text{HFA}} = 45\ 10^3$ Hz, $k_{\text{HFA}} a/\pi = 30$ ($a = 0.5$ m), $k_{\text{HFA}} L/\pi = 300$ ($L = 5$ m), $h = 0.0056$ m (mesh size of the most refined mesh), $N \approx 10^6$ DOFs, $M = 10^4$. The parameters for the semi-analytical approximation (C) are $M = 2048$, $N^{\theta}_{\text{modes}} = 90$ and $N^{z}_{\text{modes}} = 200$. The master mesh chosen for plots and post-processing (on which all the frequency-domain solutions are interpolated) has $7\ 10^4$ DOFs and a mesh size $h = 0.022$ m. The choice of the master mesh has very little influence on the result quality.

Figure 6 shows the total pressure p^{Ref} at three points of the cylinder surface: the standoff point A facing the explosion ($\theta = 0$, $z = 0$ with the notations of Fig. 5), the shadow point C ($\theta = \pi$, $z = 0$) opposite to A, and the orthogonal point B ($\theta = \pi/2$, $z = 0$). To avoid Gibbs phenomena associated to discontinuous inputs, the time variation of the incident pressure is modified so as to vary smoothly from zero to its maximum during a small time interval (typically set to $\tau/20$ or $\tau/10$, where τ refers to the exponential time constant related to the explosion), a customary treatment in underwater explosion analysis. In particular, this implies that the input is regular enough to formulate the BEM problems for the pressure, instead of the velocity potential. The fast $\mathcal{Z}$-BEM and the semi-analytical method are seen in Fig. 6 to provide very similar results (with the $\mathcal{Z}$-BEM solution at the shadow point C exhibiting small non-physical perturbations that slightly affect the overall solution).

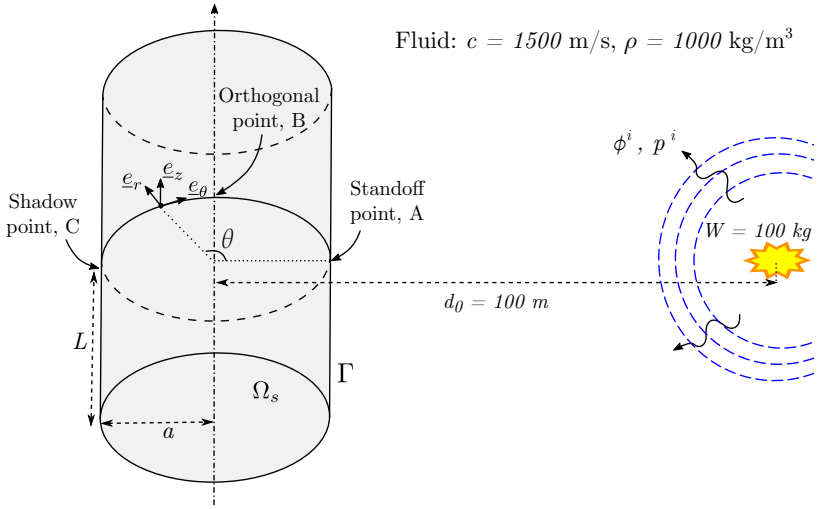

FIGURE 5 Infinite cylinder facing an underwater explosion.

TABLE 2 Scattering by a small cylinder ($a = 0.5$ m, $L = 5$ m): influence of f_{HFA} on time-domain solution accuracy (with $k_{\mathrm{HFA}} = 2\pi f_{\mathrm{HFA}}/c$). The pointwise relative difference indicator δ is defined by (41).

f_{HFA} (kHz)	$k_{\mathrm{HFA}}a/\pi$	$k_{\mathrm{HFA}}L/\pi$	M_B	$\delta(\mathbf{x})$ (%)		
				$\mathbf{x}=A$	$\mathbf{x}=B$	$\mathbf{x}=C$
20.0	13.3	133	32	4.9	3.6	9.4
25.0	16.7	167	40	4.8	3.4	8.3
30.0	20.0	200	48	4.7	3.4	8.0
35.0	23.3	233	56	4.7	3.3	7.6
40.0	26.7	267	64	4.7	3.3	7.5
45.0	30.0	300	72	4.7	3.3	7.4

Table 2 illustrates the influence of f_{HFA} on the accuracy in the time domain of the solution at the standoff, orthogonal and shadow points, in terms of the relative pointwise solution error

$$\delta(\mathbf{x}) := \frac{\|p(\mathbf{x},\cdot) - p_{\mathrm{ex}}(\mathbf{x},\cdot)\|_{L^2([0,T])}}{\|p_{\mathrm{ex}}(\mathbf{x},\cdot)\|_{L^2([0,T])}} \tag{41}$$

for the acoustic time-dependent pressure response $p(\mathbf{x},\cdot)$ evaluated at a point $\mathbf{x} \in \Gamma$. The trends are similar to those observed for the pulsating sphere example (see Table 1); in particular, the solution errors decrease as f_{HFA} increases. This indicates that the enhanced HFA we designed for the scattering case is efficient for cylindrical geometries. Note that the solution accuracy is estimated with p_{ex} taken as the semi-analytical solution, which also only approximates the exact solution due to various factors such as series truncations. The time-domain solution $t \mapsto p^{\mathrm{Ref}}(A,t)$ at the standoff point is almost optimal with $M_B = 32$ BEM solutions, as adding more BEM solutions only slightly reduces the solution error. The same observation holds for $t \mapsto p^{\mathrm{Ref}}(B,t)$. The solution appears to be most accurate in this region ($\theta \approx \pi/2$), which makes our HFA attractive because this is precisely the case where the classical Kirchhoff approximation is least accurate. At the shadow point, non-physical oscillations appear once p^{inc} reaches that point. The magnitude of these oscillations reduces as f_{HFA} increases, which makes sense since they are caused by insufficient accuracy when using the HFA at frequencies not high enough.

By contrast with Sec. 4.1, differences between BEM and HFA solutions are not provided in Table 2, since they are zero by construction for $|s| = f_{\mathrm{HFA}}$, see Sec. 3.4. The HFA quality in the scattering case depends on whether the ratio (34) is stable as $|s|$ increases. This behavior varies according to the location on the surface, as illustrated on Fig. 7, and appears from a comparison with Table 2 to be correlated with the overall time-domain solution accuracy.

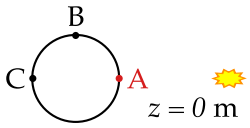

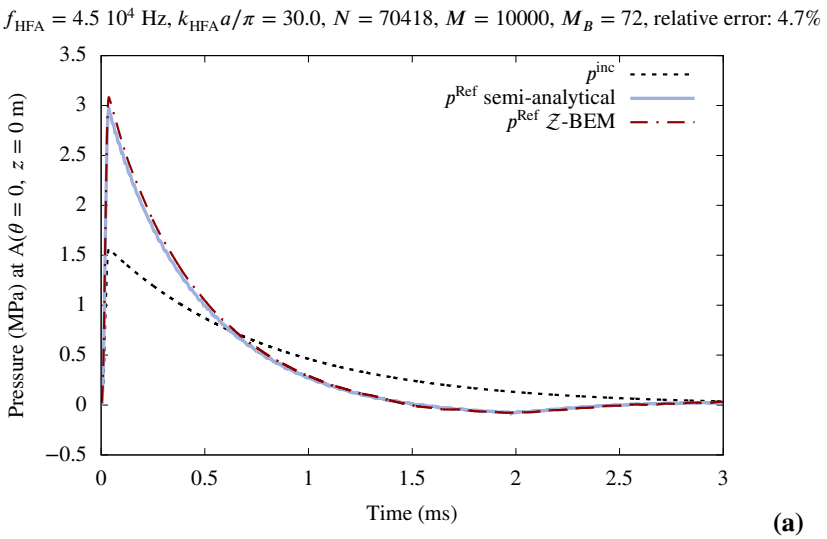

(a)

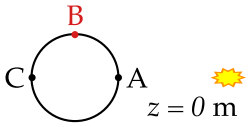

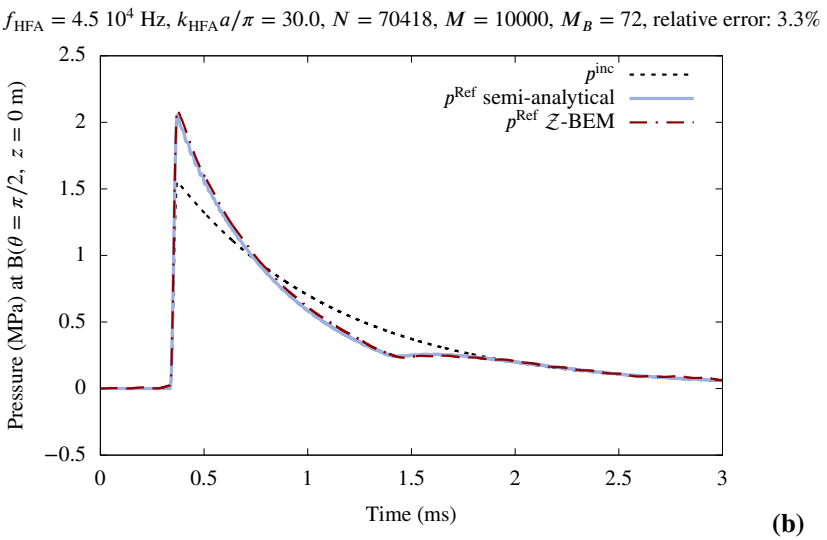

(b)

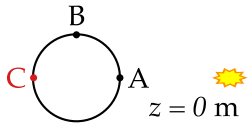

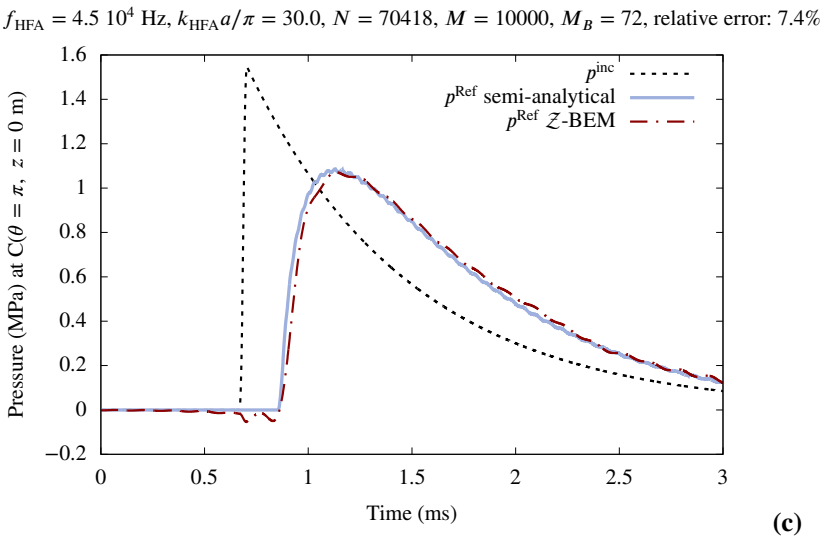

(c)

FIGURE 6 Scattering by a small cylinder ($a = 0.5$ m, $L = 5$ m, see Fig. 5): comparison between the $\mathcal{Z}$-BEM and semi-analytical solutions for the total field p^{Ref} on the $z = 0$ plane, at the standoff (a), orthogonal (b) and shadow (c) points. The incident field at those points is also shown.

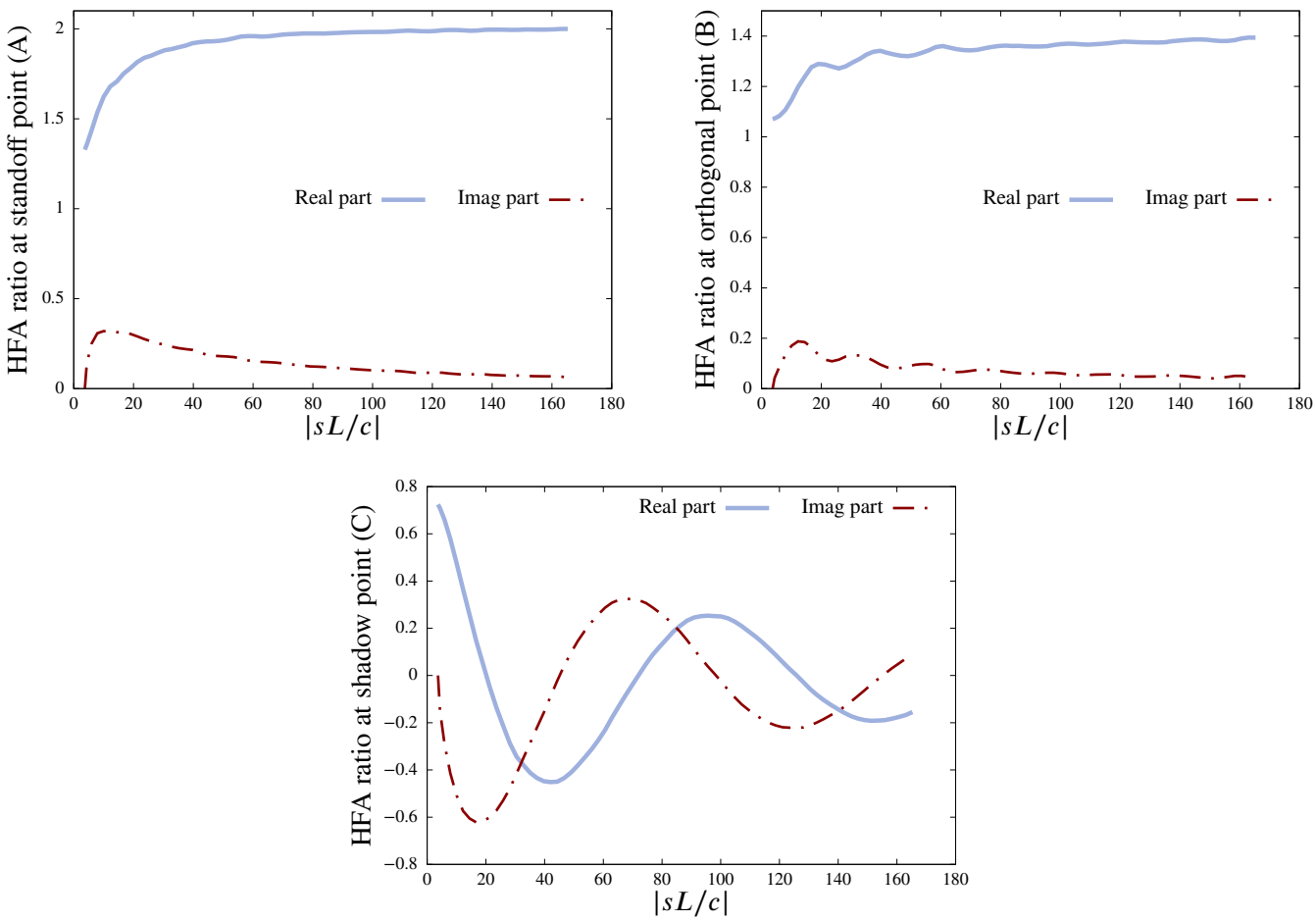

FIGURE 7 Scattering by a small cylinder ($a = 0.5\,\text{m}$, $L = 5\,\text{m}$, see Fig. 5): HFA ratio $\mathcal{R}(\mathbf{y}, s)$ at standoff, orthogonal and shadow points A, B, C (defined as in Fig 6).

The results of this section, applied to a small cylinder facing an underwater explosion, validate sufficient accuracy of the proposed HFA-enhanced $\mathcal{Z}$-BEM; they also show its efficiency, since for this case only 72 BEM solutions are needed to get satisfactory results (by comparison, $O(M)$ BEM problems are needed for either a time-domain BEM or the $\mathcal{Z}$-BEM without HFA).

4.3 | Example involving premature onset of HFA.

So far, we considered cases for which computational resources allowed to solve BEM problems at any frequency below a physically reasonable HFA threshold. However, for applications such as modelling a submarine facing an underwater explosion, the size and complexity of the structure would make solving all the BEM problems failing a preset tolerance tol_{HFA} of (say) 5% too expensive. In such cases, the number of practically solvable BEM problems results from computational constraints rather than a sensible HFA threshold. Therefore, in practice, f_{HFA} is set to the highest frequency that can be dealt with by the BEM, and all problems (21) for which $|s(\xi)| \geq f_{\text{HFA}}$ are solved using a HFA, even though some of those HFA solutions will have low accuracy.

This makes it important to evaluate how a forced premature recourse to HFA affects the accuracy of the time-domain solution. To this end, we consider a variant of the configuration studied in Sec. 4.2 involving a larger cylinder, and use the following parameters: $T = 20\,\text{ms}$, $f_{\text{HFA}} = 4.5\ 10^3\,\text{Hz}$, $k_{\text{HFA}}a/\pi = 30$ ($a = 5\,\text{m}$), $k_{\text{HFA}}L/\pi = 300$ ($L = 50$ m), $h = 0.056\,\text{m}$ (mesh size of the most refined mesh), $N \approx 10^6$ DOFs, $M = 10^4$. The parameters for the semi-analytical approximation (C) are, as

before, $M = 2048$, $N^{\theta}_{\text{modes}} = 90$ and $N^{z}_{\text{modes}} = 200$. Again, we use the mesh interpolation, the master mesh used for plots and post-processing having 7 10^4 DOFs and a $h = 0.22\,\text{m}$ mesh size.

The total pressure p^{Ref} on Γ for this non-optimal set of parameters is presented in Figs. 8 and 9. The too-small value of f_{HFA} used results in stronger non-physical oscillations in the shadow region, yet the overall result remains satisfactory in view of the challenging problem dimensions considered since

- the overall trend of the solution is correct;
- in the shadow zone, the non-physical oscillations occur about a mean value that corresponds to the correct solution.

The advantage of our method is then to obtain an accurate enough solution under challenging conditions that might prevent other numerical methods to perform. The loss of accuracy induced by forced premature recourse to HFA depends on the limitation of computational resources. The influence of f_{HFA} is in addition quantitatively illustrated in Table 3, corroborating the above-mentioned trends. The $O(1)$ complexity in time afforded by the HFA (see Sec. 3.5) is demonstrated for this example in Table 4, which shows the evolution of M_B in the cylindrical cases presented in this article, obtained using the backward differential formula of order 2.

Figure 10 illustrates the HFA ratio in the case of the large cylinder, it shows similar behaviour as in the small cylinder case (see Fig. 7).

TABLE 3 Scattering by a large cylinder ($a = 5\,\text{m}$, $L = 50\,\text{m}$): influence of f_{HFA} on time-domain solution accuracy (with $k_{\text{HFA}} = 2\pi f_{\text{HFA}}/c$). The pointwise relative difference indicator δ is defined by (41).

f_{HFA} (kHz)	$k_{\text{HFA}}a/\pi$	$k_{\text{HFA}}L/\pi$	M_B	$\delta(\mathbf{x})$ (%)					
				$\mathbf{x}=A$	$\mathbf{x}=B$	$\mathbf{x}=C$	$\mathbf{x}=D$	$\mathbf{x}=E$	$\mathbf{x}=F$
2.0	13.3	133	13	18.7	4.9	38.6	11.9	4.1	36.8
2.5	16.7	167	16	13.8	4.1	23.1	9.6	3.5	22.8
3.0	20.0	200	20	9.8	3.5	22.5	7.4	3.2	21.2
3.5	23.3	233	23	7.8	3.2	18.3	6.5	3.1	16.8
4.0	26.7	267	26	6.8	3.3	15.2	5.6	3.1	14.3
4.5	30.0	300	29	6.1	3.4	13.7	5.3	3.1	12.3

TABLE 4 Scattering by a large cylinder ($a = 5\,\text{m}$, $L = 50\,\text{m}$, see Fig. 5): demonstration of the $O(1)$ time complexity of the procedure.

Cyl diameter (m)	f_{HFA} (kHz)	T (ms)	M	M_B	Estimate (36)
1.0	45.0	5.0	10^2	52	80
			10^3	76	
			10^4	77	
			10^5	77	
10.0	4.5	20.0	10^2	25	32
			10^3	29	
			10^4	29	
			10^5	29	

To conclude, since the computational complexity of our procedure is $O(N \log N)$ with regards to the number of spacial DOFs N, and $O(1)$ with regards to the number of time steps M, future improvements in computing resources will benefit our procedure more than other procedures with higher complexity.

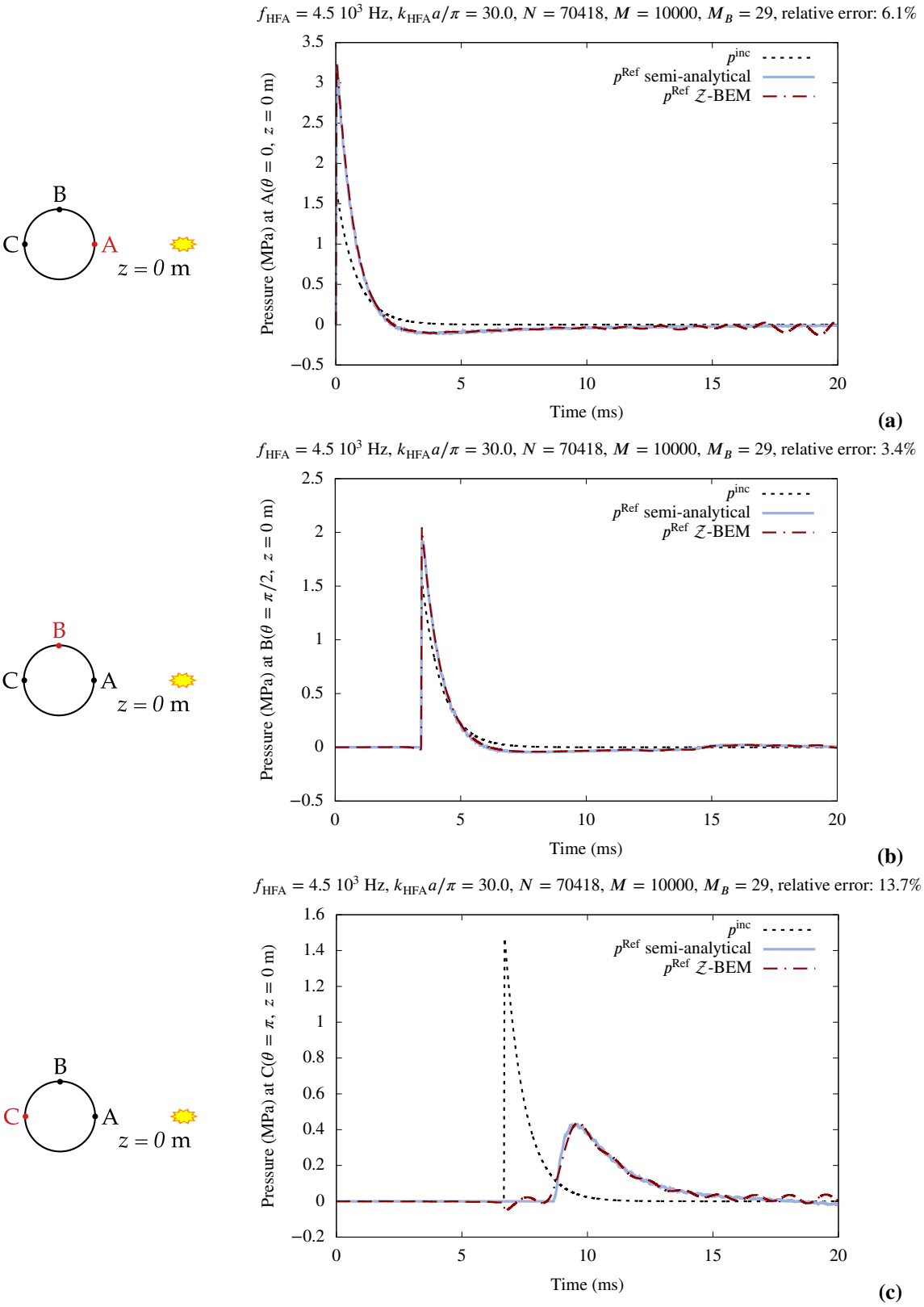

FIGURE 8 Scattering by a large cylinder ($a = 5$ m, $L = 50$ m, see Fig. 5): comparison between the $\mathcal{Z}$-BEM and semi-analytical solutions for the total field p^{Ref} on the $z = 0$ plane, at the standoff (a), orthogonal (b) and shadow (c) points. The incident field at those points is also shown.

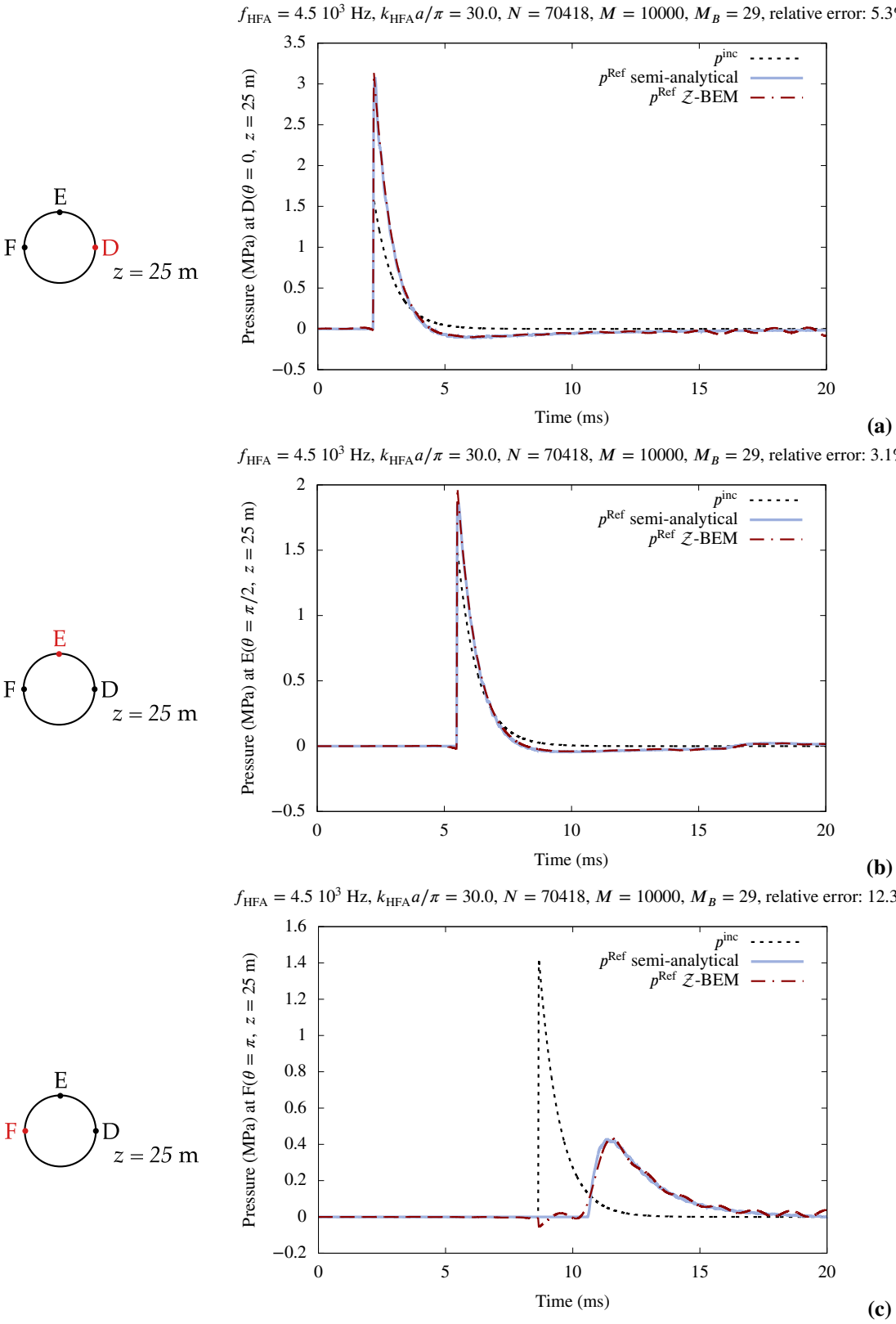

FIGURE 9 Scattering by a large cylinder ($a = 5$ m, $L = 50$ m, see Fig. 5): comparison between the $\mathcal{Z}$-BEM and semi-analytical solutions for the total field p^{Ref} on the $z = 25$ m plane, at the standoff (a), orthogonal (b) and shadow (c) points. The incident field at those points is also shown.

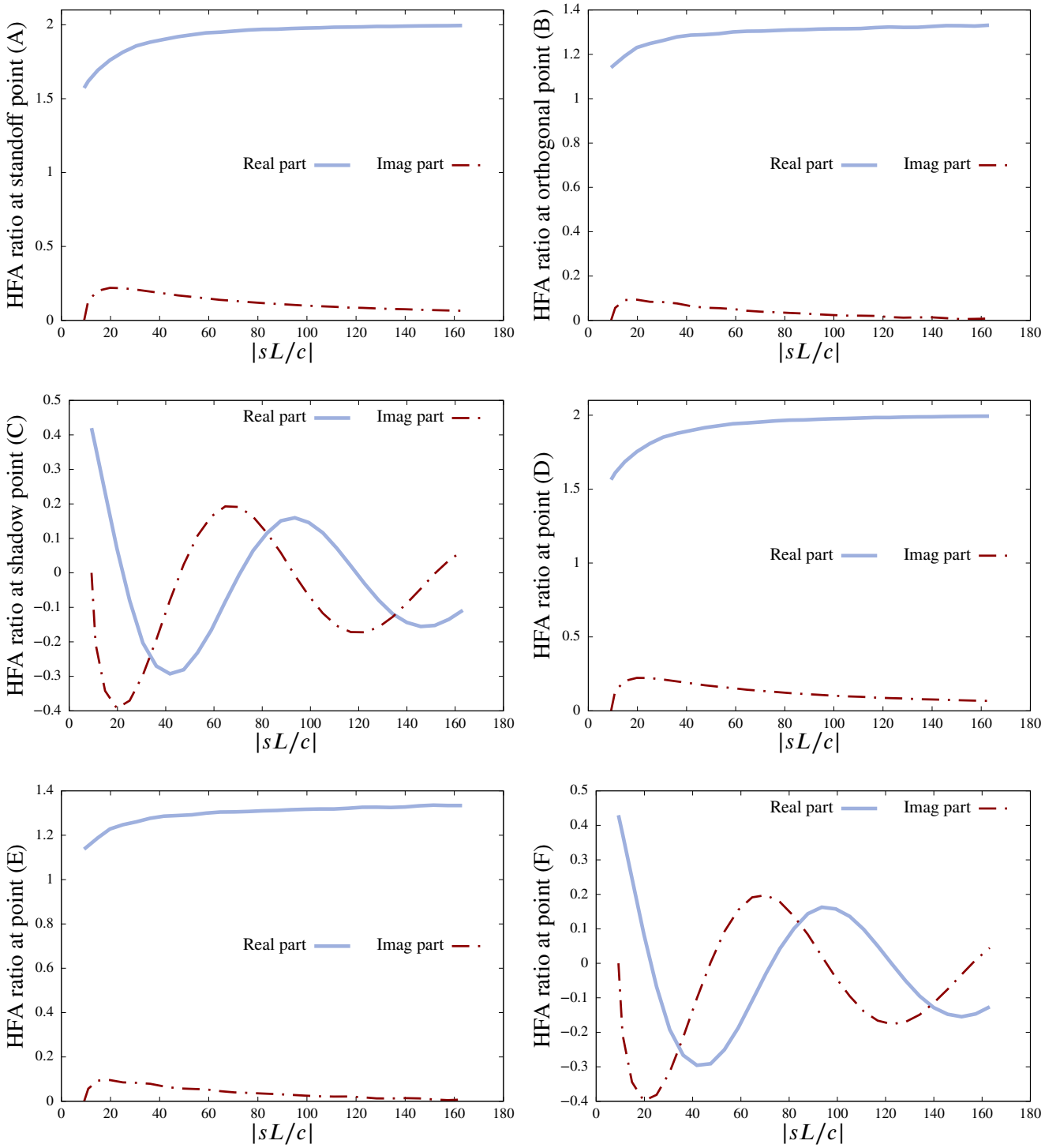

FIGURE 10 Scattering by a large cylinder ($a = 5\,\text{m}$, $L = 50\,\text{m}$, see Fig. 5): HFA ratio.

5 | SCATTERING OF A SPHERICAL WAVE BY A RIGID MOTIONLESS COMPLEX STRUCTURE

This final section demonstrates the efficiency of the fast $\mathcal{Z}$-BEM procedure for the three-dimensional scattering of a spherical wave by a complex submarine-shaped structure referred to as BB2. Its geometry, provided in [50], corresponds to a realistic submarine of length 70.2 m and height 16.4 m. It is composed of three main parts: the beam (cylindrical hull), the sail, and the planes (2 sail planes, 4 back planes). The propeller has been removed from the geometry and is not modelled.

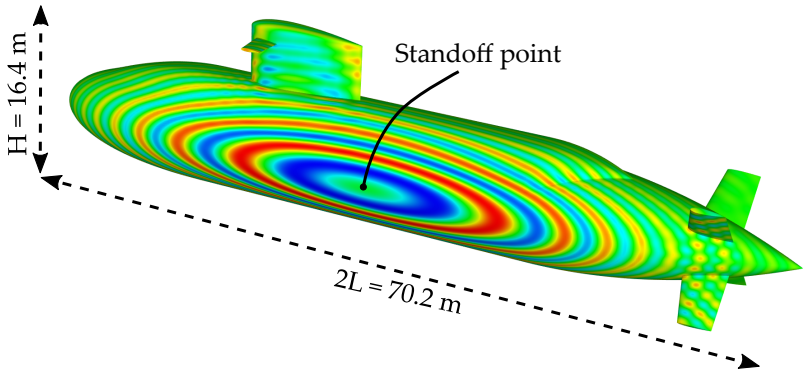

FIGURE 11 Scattering by a rigid motionless submarine: $\mathcal{Z}$-transform of the total pressure $P^{\text{Ref}}(s)$ on the submarine surface, with $sL/c \approx 6.01 + 166\text{i}$.

The BB2 is assumed to be motionless, and faces an explosion of $W = 100$ kg of TNT located 100 m away from the submarine center. The standoff point is located on the beam; it is at the center of the concentric ellipses in Fig. 11. The main goal is to compute the total pressure field p^{Ref} on the submarine surface Γ. As before, the $\mathcal{Z}$-BEM procedure entails the solution of a large number of frequency-domain problems, using either the FM-BEM or a HFA. For the FM-BEM, 7 meshes are defined, with regular decreasing mesh size. The master mesh, used for interpolation, has $N \approx 3\ 10^5$ DOFs, corresponding to a mesh size of $h = 0.1$ m. The most refined mesh has $N \approx 3\ 10^6$ DOFs, corresponding to a mesh size of $h = 0.03$ m. Since N is large, f_{HFA} and M_B are set as explained in Sec. 4.3. For a given frequency $s(\xi_k)$, the associated BEM problem is solved using the least refined mesh that has at least 8 points per wavelength, except for the finest mesh, which is used with at least 6 points per wavelength. The latter restriction results in $f_{\text{HFA}} = 8.667$ kHz (i.e., $k_{\text{HFA}} L/\pi = 417$) and $M_B = 56$.

5.1 | Frequency-domain BEM performance.

The characteristics of a sample of the 56 BEM solution evaluations are provided in Table 5. As $|s|$ increases, the iterative BEM procedure behaves as expected on several respects. In particular, the number of FMM levels slowly increases (up to 8), while the GMRES iteration count also increases with N and $|s|$. The latter however remains moderate for all used frequencies, despite the geometrical complexity; this is due to the use of complex frequencies, which implies a spatially-decaying factor $e^{-\text{Re}(s)r/c}$ in the fundamental solution, thereby reducing the effect of far contributions and improving the condition number of the BEM matrices. For GMRES, we avoided using initial guesses that depend on previously-obtained solutions (at lower frequencies), as this allows all BEM solutions to be computed concurrently, i.e., full parallelism for this part of the process. The elapsed time for the whole transient analysis thus depends directly on the number of computers (nodes) available. Here, the computations were run on a single machine with a 3.5GHz Intel XEON E5-2637 v3 processor, 8 cores, 2 chips, 4 cores/chip, 2 threads/core, and 768 GB of RAM.

TABLE 5 Scattering by a rigid motionless submarine: characteristics of some of the frequency-domain BEM solution evaluations ($\mathrm{Re}(sL/c) = 6.0$).

N	$\mathrm{Im}(sL/c)$	**# of levels**	**GMRES iters.**	**Pts per λ**
155 083	26.43	5	20	9.0
530 021	56.63	6	28	8.8
1 048 115	64.18	7	29	11.1
	86.83	7	30	8.2
2 787 749	109.49	8	31	11.4
	139.70	8	32	8.9
	154.80	8	33	8.1
	177.47	8	34	7.0
	185.02	8	35	6.8
	192.57	8	36	6.5
	200.12	8	37	6.2
	207.68	8	38	6.0

5.2 | HFA, time-domain results.

We now assess the HFA proposed in Sec. 3.4 on this example, which features a complex geometry; in particular, Γ is not convex, implying that Kirchhoff-type approximations no longer have theoretical justification. Figure 12 shows the HFA ratio $\mathcal{R}(\mathbf{y}, s)$ (see (34)) at various points $\mathbf{y}$ as a function of $|s|$. On the cylindrical hull of the submarine, the ratio is stable (like for the cylinder case). In regions with more-complex local geometry, typically near the submarine planes or between two plates (where waves are trapped), $s \mapsto \mathcal{R}(\mathbf{y}, s)$ is oscillatory. This observation is reinforced by Figure 13, which reveals the regions of the submarine surface where $s \mapsto \mathcal{R}(\mathbf{y}, s)$ is not stable by plotting the relative oscillation $\mathbf{y} \mapsto \Delta_{\mathrm{HFA}}(\mathbf{y})$ over the last third of the set of M_B BEM frequencies, defined by

$$\Delta_{\mathrm{HFA}}(\mathbf{y}) = \frac{1}{2} \frac{\max\limits_{k \in J} \left(\mathcal{R}(\mathbf{y}, s_k) \right) - \min\limits_{k \in J} \left(\mathcal{R}(\mathbf{y}, s_k) \right)}{\max\limits_{k \in I} |\,\mathrm{Re}(\mathcal{R}(\mathbf{y}, s_k))| + \max\limits_{k \in I} |\,\mathrm{Im}(\mathcal{R}(\mathbf{y}, s_k))|} \tag{42}$$

with $I := [\![1, M_B]\!]$, $J := [\![2M_B/3, M_B]\!]$ and where $\max(z) := \max(\mathrm{Re}(z)) + \mathrm{i}\max(\mathrm{Im}(z))$ (and similarly for $\min(z)$) for $z \in \mathbb{C}$. By construction, $0 \leq \Delta_{\mathrm{HFA}} \leq 1$. Low values of Δ_{HFA} (showing at most moderate relative variations of $s \mapsto \mathcal{R}(\mathbf{y}, s)$) occur mainly on the smooth, locally convex, parts of Γ, larger values (showing significant relative variations of $s \mapsto \mathcal{R}(\mathbf{y}, s)$ being by contrast observed near the sail and back regions, where the surface has features with smaller length scales.

Importantly, this observed behaviour of $\mathcal{R}(\mathbf{y}, s)$ is consistent with the expectation that HFAs of Kirchhoff type are valid in locally convex regions where the radius of curvature is moreover large relative to the characteristic wavelength. The validity of HFAs in regions of complex geometry would entail both an as yet unknown HFA method and values of f_{HFA} well beyond the current capabilities of the frequency-domain BEM for this configuration. We nonetheless tried our heuristic approach to HFA on the submarine surface, to observe its effect on the overall result.

The number $M_B = 56$ of frequency-domain BEMs to be solved is very small compared to the $M + 1 = 10001$ frequency-domain BEMs that would be solved without using a HFA. Figure 14 shows how the frequencies for which a BEM problem is solved are concentrated near the origin in the complex s-plane. The real part of these frequencies (attenuation part) is almost constant ($\mathrm{Re}(s) \approx 6.0$), whereas their imaginary part (oscillatory part) grows from 0 to the limit fixed by f_{HFA}.

Figure 15 shows the computed surface pressure field 5.4 milliseconds after the incident wave first hits the submarine. The quality of the computation is illustrated by the smooth wave front, propagating on the beam. In the shadow zone, the causality of the wave is respected (the total field needs more time than the incident field to reach points in the shadow zone). In the back region of the submarine, planes trap waves and multiple reflexions are accordingly observed. The quality of the computed wave front is somewhat reduced in the trapping region, as two small unphysical spots appear, presumably as a result of applying a HFA in a region whose complexity makes it invalid at the frequencies used, as previously observed in cases (d,e,f) of Fig. 12.

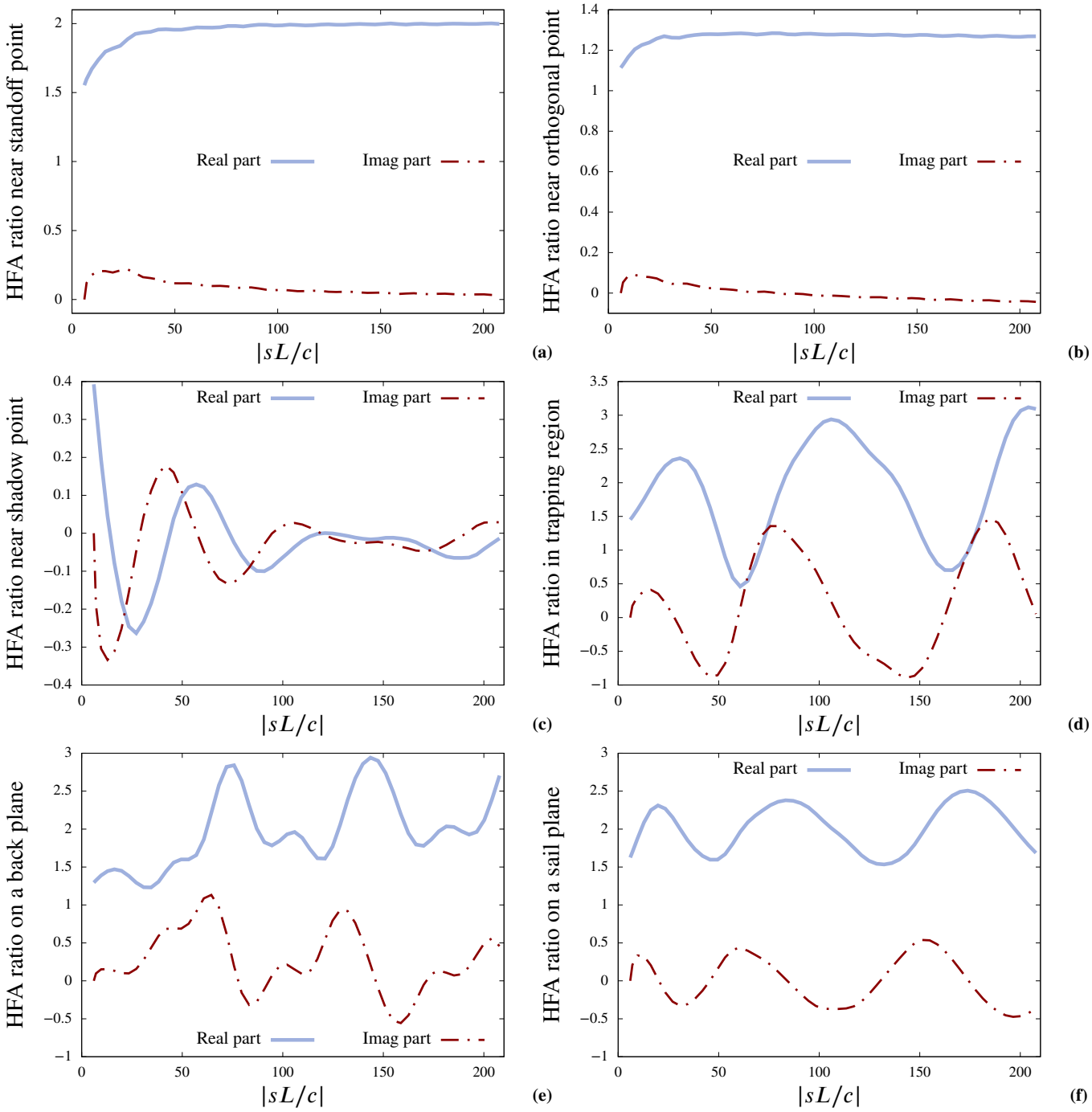

FIGURE 12 Scattering by a rigid motionless submarine: behaviour of the HFA ratio.

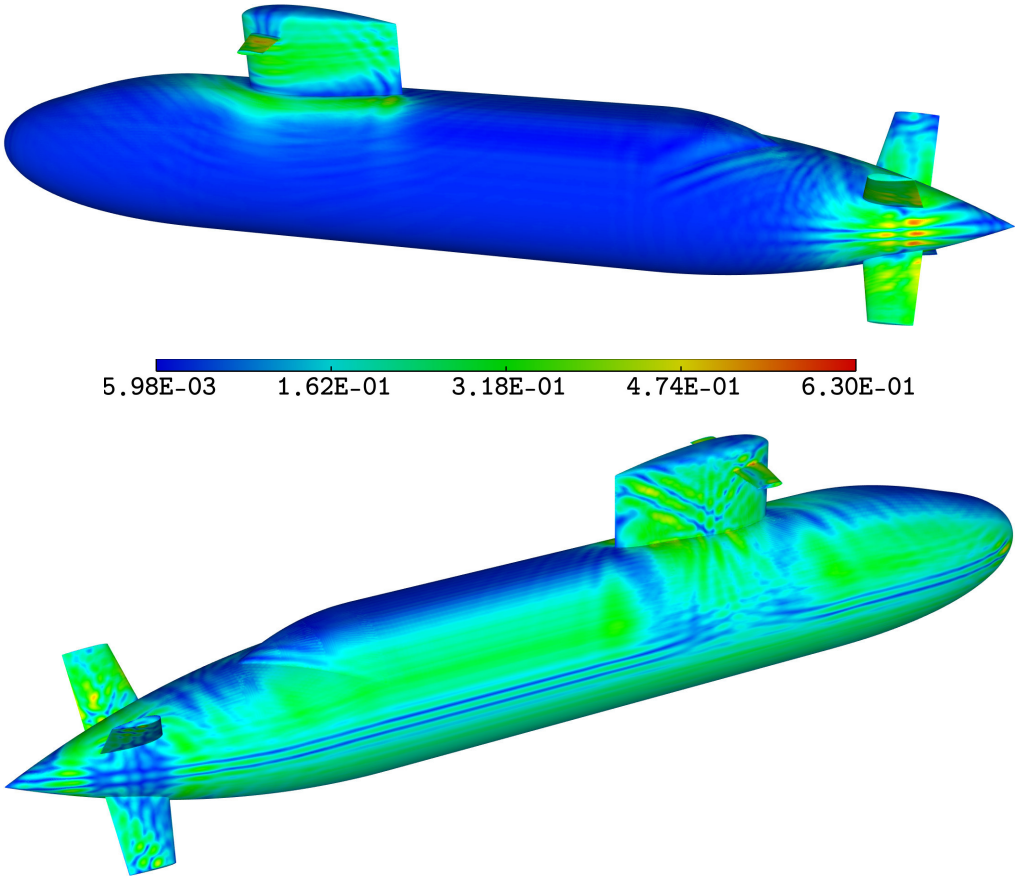

FIGURE 13 Scattering by a rigid motionless submarine: relative oscillation $\Delta_{\text{HFA}}(\mathbf{y})$ of $\mathbf{y} \mapsto \Delta_{\text{HFA}}(\mathbf{y})$ plotted as a function of $\mathbf{y} \in \Gamma$. BEM solutions for $M_B = 56$ complex frequencies were computed.

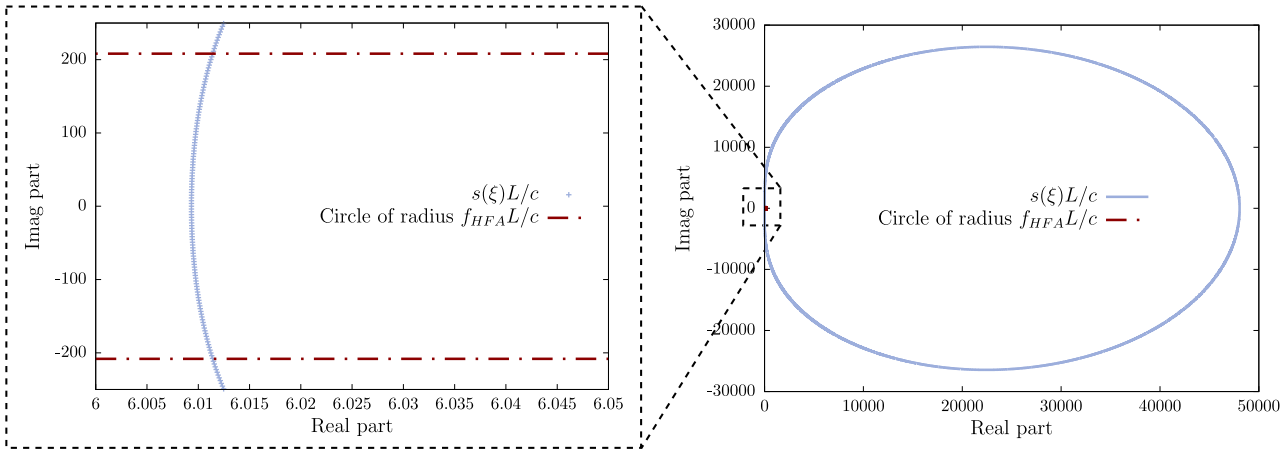

FIGURE 14 Scattering by a rigid motionless submarine: complex frequencies sL/c used by the $\mathcal{Z}$-BEM. The frequencies for which a BEM problem is solved are concentrated near the origin.

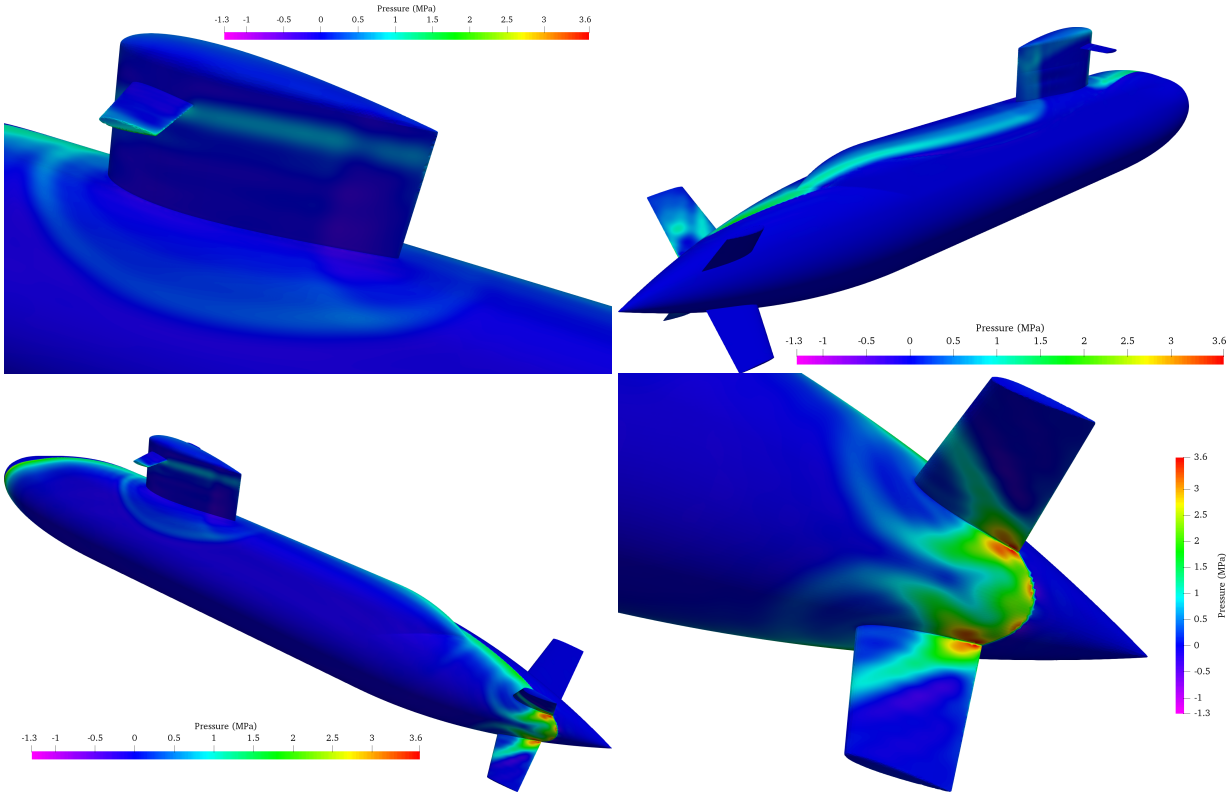

FIGURE 15 Scattering by a rigid motionless submarine: total pressure field on the surface, 5.4 milliseconds after the incident wave first hits the submarine.

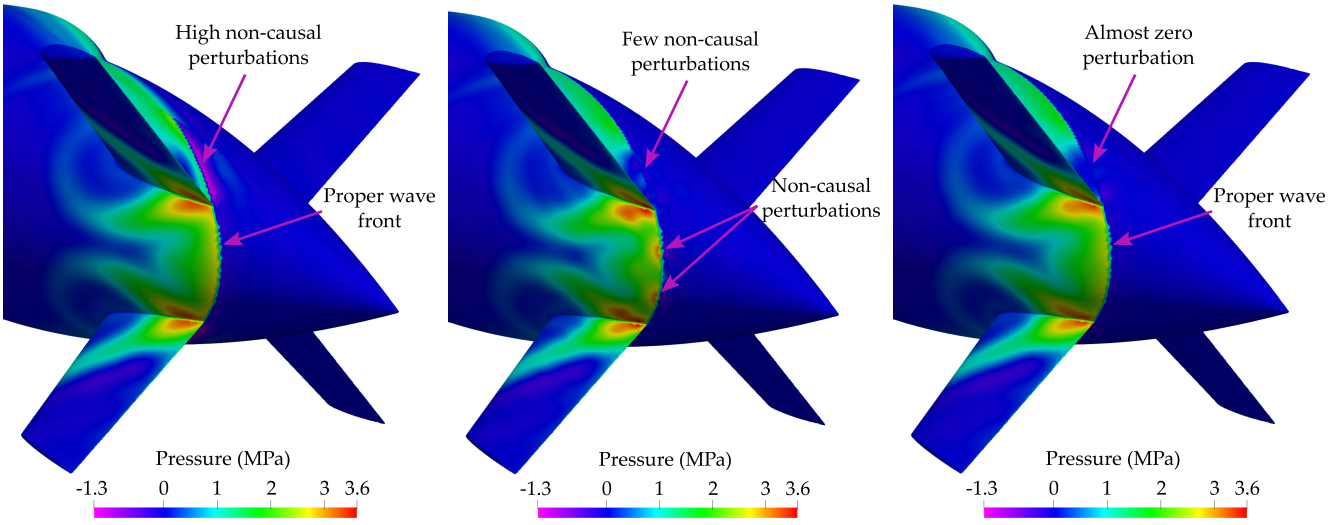

FIGURE 16 Scattering by a rigid motionless submarine: total pressure field on the surface, 5.4 milliseconds after the incident wave first hits the submarine. Close-up on the back part for three variants of the HFA, based on the Kirchhoff approximation (left), $\mathcal{R}(\mathbf{y}, s_{\mathrm{HFA}})$ (middle) or an average of $\mathcal{R}(\mathbf{y}, \cdot)$ (right).

There is obviously much room for improvement in, and deeper investigation into, the design and justification of more elaborate and accurate HFAs, with expected benefits to solution accuracy reachable within moderate M_B. For now, we tried a simple modification where $\mathcal{R}(\mathbf{y}, s_{\text{HFA}})$ is replaced by its mean value over s, for $|s| \in [0, f_{\text{HFA}}]$, when $\Delta_{\text{HFA}}(\mathbf{y}) > 0.1$ (see (42) and Fig. 13); i.e., for the points where $\mathcal{R}(\mathbf{y}, s)$ is not constant yet. We compare in Fig. 16 the pressure field obtained in the back region of the submarine using three versions of the HFA, based on (i) the Kirchhoff approximation (33), (ii) $\mathcal{R}(\mathbf{y}, s_{\text{HFA}})$, and (iii) a frequency-averaged value of $\mathcal{R}(\mathbf{y}, \cdot)$. For version (i), the total pressure field is well represented in the trapping region, where $\mathcal{R}(\mathbf{y}, s) = 2$ defines a suitable approximation. However, it leads to non-physical perturbations behind back planes, with pressure showing negative and positive peaks whereas it should vanish by causality. If used for subsequent FSI analyses, this pressure input may deteriorate overall FSI solutions in regions with complex geometry due to induced non-physical deformations. With version (ii), the pressure solution in the region behind the back plane is improved. However, perturbations appear at the wave front in the trapping region, as two non-physical (non-causal) spots appear; they are due to a value of f_{HFA} that is locally too low, see cases (d,e,f) of Fig. 12. Finally, using version (iii) in the geometrically complex regions identified in Fig. 13 produces a correct wave front in the trapping region (its peak value being however lower than that obtained using the Kirchhoff HFA) and removes non-physical pressure jumps behind the back plane.

6 | CONCLUSIONS AND FUTURE WORK

The main purpose of this work was to design and implement a BEM-based numerical procedure that can solve large-scale 3D rapid transient acoustic problems. We first illustrated the efficiency of our $\mathcal{Z}$-BEM procedure, based on the $\mathcal{Z}$-transform and the use of a HFA, in the case of rapid transient radiation problems, in Sec. 4.1. Then, we addressed the scattering case, where an *ad hoc* HFA was designed, in Sec. 4.2. This empirically constructed HFA was shown in Sec. 5 to remain effective for dealing with large complex geometries. Finally, since the complexity of the $\mathcal{Z}$-BEM procedure is $O(1)$ in regards to the time discretisation and $O(N \log N)$ for the spacial discretisation, it ranks among the most competitive available methods.

Our longer-term goal is to develop a coupled BEM-FEM approach for the complete fluid-structure interaction (FSI) problem, a natural approach when the surrounding medium can, as here, be considered as unbounded. FEM-BEM coupling is for instance used in soil-structure interaction [16,51] or in FSI, see e.g., [52,53,54] on the effect of underwater explosions on shells. In the present $\mathcal{Z}$-BEM framework that forces time-domain solutions to be computed at once over the whole time interval of interest, developing a convergent iterative algorithm that alternates time-domain BEM (fluid) solutions and FEM (structure) solutions remains a significant issue which we are currently investigating. The rigorous formulation of HFAs that take advantage of the spatial attenuation afforded by the complex-frequency framework, and their optimal inclusion into the $\mathcal{Z}$-BEM framework, constitutes another important topic of future investigation, even more so if such HFAs can be given theoretical justification for non-convex obstacles.

□

APPENDIX

A FAST MULTIPOLE ACCELERATED BOUNDARY ELEMENT METHOD

To present the FMM concept, it is instructive to go back to its original application, namely the N-body problem in physics [55,56]. Consider a set of many particles in mutual interaction through a cohesive force whose potential is inversely proportional to the inter-particle distance (denoted r thereafter). The idea is as follows [55,56,57]: due to the spatial decay of the potential, the interaction between two well-separated sets $\{\mathbf{x}_i\}$ and $\{\mathbf{y}_j\}$ of particles can be roughly approximated by the interaction between the set centres $\mathbf{x}_g, \mathbf{y}_g$ carrying the net charges (Fig. A1), acting as monopoles. This approximation (and its refinements involving multipoles) in particular separates the variables $\mathbf{x}, \mathbf{y}$.

For wave propagation, the fundamental solution has to be reformulated in such a way that the $\mathbf{x}$ and $\mathbf{y}$ variables ($r = \|\mathbf{x} - \mathbf{y}\|$) are separated. Using the notations of Fig. A1, the position vector $\mathbf{r}$ is expressed as $\mathbf{r} = \mathbf{r}_g + (\mathbf{y} - \mathbf{y}_g) - (\mathbf{x} - \mathbf{x}_g)$, where $\mathbf{r}_g = \mathbf{y}_g - \mathbf{x}_g$. Then, the fundamental solution (19) admits the decomposition [21,58]:

$$\bar{G}(r, s) = \lim_{L \to +\infty} \int_{\hat{\boldsymbol{\alpha}} \in S} e^{s\, \hat{\boldsymbol{\alpha}} \cdot (\mathbf{x} - \mathbf{x}_g)/c} \mathcal{G}_L(\hat{\boldsymbol{\alpha}}; \mathbf{r}_g; s) e^{-s\, \hat{\boldsymbol{\alpha}} \cdot (\mathbf{y} - \mathbf{y}_g)/c} \, \mathrm{d}\hat{\boldsymbol{\alpha}}\,, \tag{A1}$$

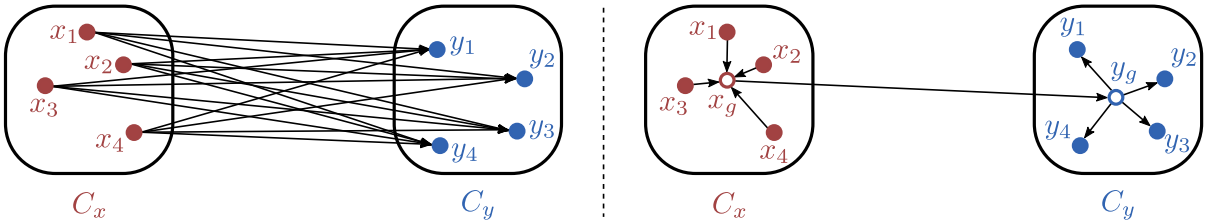

FIGURE A1 Illustration of the FMM concept, actions of the particules in a cell C_x (centre x_g) on the particules in a cell C_y (centre y_g). Left: without FMM, right: with FMM.

where $\mathcal{S}$ denotes the unit sphere of $\mathbb{R}^3$, and $\mathcal{G}_L$ is a transfert function defined in terms of the modified spherical Bessel functions k_p [59, Chap. 10] and the Legendre polynomials P_p [59, Chap. 18] by

$$\mathcal{G}_L(\hat{\boldsymbol{\alpha}}; \mathbf{r}_g; s) = \frac{s}{16\pi^2 c} \sum_{0 \le p \le L} (2p+1) i^p \mathsf{k}_p(s r_g / c) P_p(\cos(\hat{\boldsymbol{\alpha}}, \mathbf{r}_g)) \,. \tag{A2}$$

The decomposition (A1) achieves the desired separation between the variables $\mathbf{x}$ and $\mathbf{y}$. When inserted into a boundary integral equation like (21), it allows to approximate the integral. However, it is valid only for well separated sets of points $\mathbf{x}, \mathbf{y}$.

Single-level FMM

The boundary Γ is enclosed in a set of cubic cells of equal size (see Fig. A2 for a 2D depiction). For a chosen point $\mathbf{y} \in \Gamma$, let C_y denote the cell containing $\mathbf{y}$. The adjacent cell set, $\mathcal{A}(C_y)$ comprises those cells sharing at least a common vertex with C_y that intersect Γ. Any cell C not belonging to $\mathcal{A}(C_y)$ is well-separated from C_y. This single-level algorithm solves (25) iteratively, with evaluations of $[\mathbf{K}]\{\mathbf{v}\}$ combining adjacent and far contributions. The latter are computed using the decomposition (A1), while the former use standard matrix-vector products. This algorithm evaluates $[\mathbf{K}]\{\mathbf{v}\}$ with a $O(N^{3/2})$, sub-optimal, complexity.

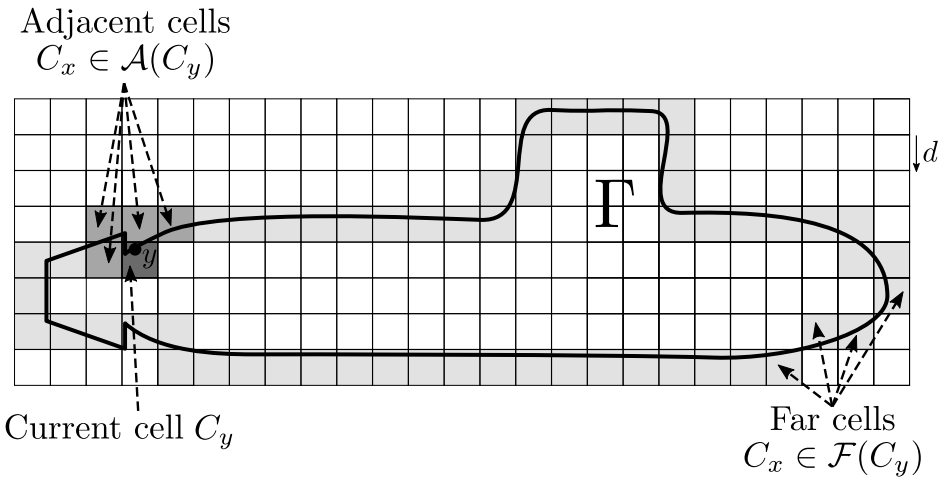

FIGURE A2 Two-dimensional grid embedding the boundary Γ. Definition of adjacent and far cells.

Principle of the multi-level FMM

The idea of the multi-level FMM is to reduce the complexity of the single-level FMM by increasing the size of far cells whenever possible, while reducing the near-interaction part of the evaluation. The multi-level FMM is driven by a recursive *octree*:

- The largest cubic cell contains Γ; it defines the *tree root* (level $\ell = 0$) of the octree.
- Level $\ell = 1$: it is composed of the 8 children cells of the tree root, the latter being their *parent cell*. The level-1 cells are all adjacent, so the FMM cannot yet be applied.

- Level ℓ is composed of at most 8^ℓ cells (cells that do not intersect Γ being discarded).
- The last level $\bar{\ell}$, implicitly defined by a preset subdivision-stopping criterion, is made of *leaf cells*.

The speed-up process is applied at each level from level $\ell = 2$ to level $\ell = \bar{\ell}$. It works by using clusters that are largest (i.e., of smallest level ℓ) whenever possible, to derive the maximum possible benefit from the decomposition (A1). To this purpose, the notion of interaction list is defined. Consider a point $\mathbf{y}$ on Γ (see Fig. A3). This point belongs to a level-2 cell denoted $C_y^{(2)}$. The speed-up process is then applied to the interactions between $C_y^{(2)}$ and all the non-adjacent level-2 cells, the latter constituting the interaction list $\mathcal{I}(C_y^{(2)})$ of $C_y^{(2)}$. At level 3, $\mathbf{y}$ belongs to a child cell $C_y^{(3)}$ of $C_y^{(2)}$. The interaction list $\mathcal{I}(C_y^{(3)})$ contains the level-3 cells not adjacent to $C_y^{(3)}$ whose parent cell belongs to $\mathcal{A}(C_y^{(2)})$. Thus, interactions are carried out level by level, until interactions between leaf cells are reached; those are computed using standard boundary element techniques. This process ensures that all contributions to $[\mathbf{K}]\{\mathbf{v}\}$ are accounted for, while taking maximum advantage from decomposition (A1).

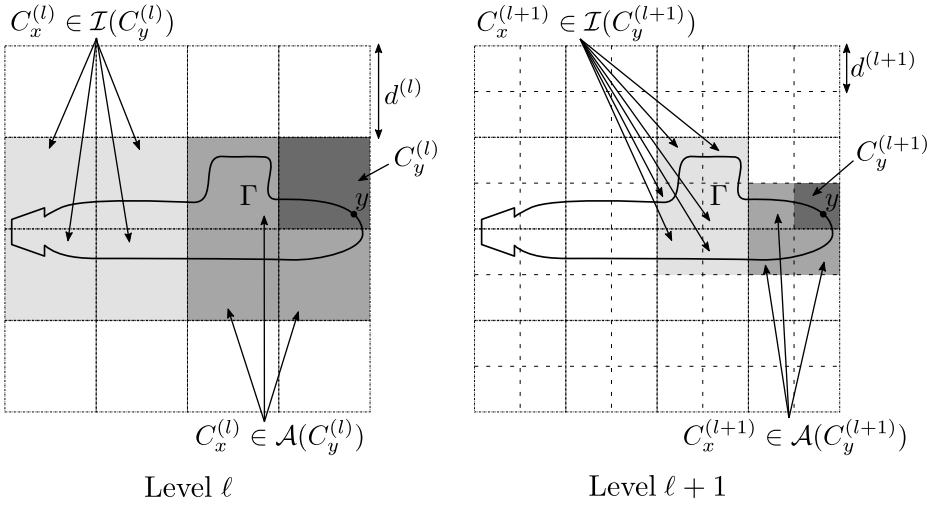

FIGURE A3 Illustration of the multi-level FMM in 2D. Both the interaction lists and the adjacent regions reduce in size as the level number increases.

B THE ACOUSTIC BREATHING SPHERE: ANALYTICAL SOLUTION

In this appendix, the (radially symmetric) analytical solution of the breathing sphere is derived in a convenient format, following classical techniques (see. e.g.[40].) The notations defined in Sec. 4.1 are used. The prescribed velocity (38) being a linear combination of data $u(t)$ of the form $u(t) = u(t;\omega) = u_0 \sin(\omega t)$ $(t \geq 0)$, it is sufficient here to consider one of such data. The Laplace transform $\bar{\phi}(r, s)$ of the velocity potential then solves the radially symmetric wave equation

$$\frac{1}{r^2}\frac{\partial}{\partial r}\left(r^2 \frac{\partial \bar{\phi}}{\partial r}\right) = \frac{s^2}{c^2}\bar{\phi}\,, \tag{B3}$$

and the boundary condition

$$\frac{\partial \bar{\phi}}{\partial r}(a, s) = \bar{u}(s) = u_0 \,\frac{\omega}{s^2 + \omega^2}, \tag{B4}$$

and vanishes as $r \to \infty$; a straightforward derivation yields the solution

$$\bar{\phi}(r, s) = -\frac{a^2\, e^{sa/c}}{1 + sa/c}\,\frac{e^{-sr/c}}{r}\,\bar{u}(s;\omega)\,. \tag{B5}$$

The pressure field is then

$$\bar{p}(r, s) = -\rho c\bar{\phi}(r, s) = \rho c\,\frac{sa^2}{(c + sa)r}\,e^{s(a-r)/c}\,\bar{u}(s;\omega)\,. \tag{B6}$$

In particular, we have on the surface

$$\bar{p}(a, s) = \rho c\,\frac{sa}{c + sa}\,\bar{u}(s;\omega)\,. \tag{B7}$$

The solution in the time domain can then be retrieved by inverse Laplace transformation. In particular, the pressure on the surface is

$$p(a,t) = \rho c a \mathcal{L}^{-1}\left(\frac{1}{c+sa}\right) \star (\dot{u}(t;\omega) + u(0;\omega)) = \rho c u_0\, \omega\, e^{-ct/a} \star \cos(\omega t)\,, \tag{B8}$$

where $\star$ denotes the time convolution of causal functions, defined by

$$(u \star v)(t) = \int_0^t u(t-\tau)v(\tau)\,\mathrm{d}\tau = \int_0^t v(t-\tau)u(\tau)\,\mathrm{d}\tau = (v \star u)(t)\,, \quad t \geq 0\,. \tag{B9}$$

After effecting two integrations by parts, we finally obtain

$$p(a,t) = \rho c u_0 \frac{\kappa}{1+\kappa^2}\left(\kappa \sin(\omega t) + \cos(\omega t) - e^{-\omega t/\kappa}\right), \qquad \kappa := \frac{\omega a}{c}\,. \tag{B10}$$

For a fixed value of ω, the analytical expressions (B7) and (B10) allow to assess the accuracy of the frequency-domain FM-BEM and the $\mathcal{Z}$-BEM procedure, respectively.

Remark 7. The analytical expression of $p(a,t)$ can be obtained for any prescribed velocity $u(t)$ provided the convolution in (B8) can be computed analytically. In particular, the accuracy of the procedure used in this article was checked with various choices for $u(t)$, such as a combination of cosines and sines or a delayed unit step function.

Remark 8. The limiting case $\kappa \to \infty$ in (B10) yields the high-frequency behavior of the surface pressure. We find $p(a,t) = \rho c u(t) + o(\kappa^{-1})$, which is the expected behavior for a radiation problem.

C SEMI-ANALYTICAL SOLUTION FOR A RIGID INFINITE CYLINDER

This section briefly summarizes the steps to obtain the semi-analytical solution for a rigid infinite cylinder, see e.g.[60] for more details. Consider a rigid infinite cylinder, of radius a and axis $\mathbf{e}_z$, facing the wave generated by a remote underwater explosion. The plane perpendicular to the cylinder containing the explosion locus is denoted $\mathcal{P} \equiv \{z = 0\}$ (see Fig. 5). The problem is studied for $z \in [-L, L]$, using cylindrical coordinates (r, θ, z). Using a classical separation of variables approach in (1), the incident (known) and reflected (unknown) pressures are expressed as Fourier series in z and θ:

$$p^{\mathrm{ref}}(r,\theta,z,t) = \sum_{m=0}^{\infty}\sum_{n=0}^{\infty} p^{\mathrm{ref}}_{m,n}(r,t)\cos(n\theta)\cos(\hat{m}z)\,, \tag{C11a}$$

$$p^{\mathrm{inc}}(r,\theta,z,t) = \sum_{m=0}^{\infty}\sum_{n=0}^{\infty} p^{\mathrm{inc}}_{m,n}(r,t)\cos(n\theta)\cos(\hat{m}z)\,, \tag{C11b}$$

where $\hat{m} \equiv \pi m/L$. The above decomposition implicitly assumes the pressures to be $2L$-periodic in z. For underwater explosions, the incident pressure, obtained by expressing (40) in cylindrical coordinates, is not $2L$-periodic (since it is a spherical wave). To bypass this difficulty, the problem is artificially set as periodic by considering simultaneous explosions with sources along the z direction separated by a distance $2L$ and of identical strength. Then, for a short enough duration T, the solution for $z \in [-L, L]$ results only from the source located in the $z = 0$ plane because of the finite wave velocity. Conversely, for a chosen time interval $[0, T]$, the length L, which may be arbitrarily chosen, must be set large enough so that the solution for $z \in [-L, L]$ is not influenced by the other sources.

Using the expression of the Laplacian in cylindrical coordinates, the wave equation for the Laplace transforms $\bar{p}^{\mathrm{ref}}_{m,n}(\cdot, s)$ of the reflected pressure reads

$$\left[\frac{\partial^2}{\partial r^2} + \frac{1}{r}\frac{\partial}{\partial r} - \left(\frac{n^2}{r^2} + k_m^2\right)\right]\bar{p}^{\mathrm{ref}}_{m,n} = 0\,, \qquad m, n \geq 0\,, \tag{C12}$$

with $k_m := \sqrt{\hat{m}^2 + s^2/c^2}$. The solution to (C12) that decays as $r \to \infty$ and satisfies the boundary condition

$$\frac{\partial \bar{p}^{\mathrm{ref}}_{m,n}}{\partial r}(a,s) = -\frac{\partial \bar{p}^{\mathrm{inc}}_{m,n}}{\partial r}(a,s) \tag{C13}$$

is given by

$$\bar{p}^{\mathrm{ref}}_{m,n}(r,s) = -\frac{1}{k_m}\frac{\partial \bar{p}^{\mathrm{inc}}_{m,n}}{\partial r}(a,s)\frac{K_n(k_m r)}{K_n'(k_m a)}\,, \tag{C14}$$

where K_n denotes the modified Bessel function of the second kind, of order n[59, Chap. 10]. The semi-analytical expression of $\bar{p}^{\mathrm{ref}}$ is then obtained by inserting (C14) into (C11a). The semi-analytical solution does **not** in practice provide exact values: its accuracy is often much lower than the machine precision and depends on many factors. The steps of the semi-analytical method are

- Perform a fast numerical Laplace transform of p^{inc}, or use an analytical expression;
- Decompose $\bar{p}^{\text{inc}}$ as a truncated series (with finite numbers $N^{\theta}_{\text{modes}}$, N^{z}_{modes} of modes);
- Compute the Fourier components of $\bar{p}^{\text{ref}}$ using (C14);
- Reconstruct $\bar{p}^{\text{ref}}$ using the truncated Fourier basis;
- Perform a fast numerical inverse Laplace transform to get p^{ref} in the time domain.

Numerical errors arise from both the fast numerical inverse Laplace transform and the fact that the Fourier basis is truncated. While not yielding an exact solution for those reasons, the semi-analytical method provides results that are accurate enough to serve as a reference for checking the validity (if not the precision) of the $\mathcal{Z}$-BEM procedure on this configuration.

Remark 9. The incident pressure given by (40) is discontinuous in time, and a Gibbs phenomenon arises near that discontinuity. To avoid nonphysical oscillations, a typical procedure, implemented in the Naval Group code that evaluates the above solution, consists in setting to zero quantities (e.g., $p^{\text{ref}}(\mathbf{x}, t)$) that are known to vanish due to causality. This improves the overall quality of the results.

References

1. Cole RH. *Underwater explosions*. Princeton University Press . 1948.
2. Snay HG. Hydrodynamics of underwater explosions. Published in *Symposium on Naval Hydrodynamics, National Academy of Sciences, Washington D.C.* 1956: 325 - 346.
3. Graham D, Hobson J, Murphy P, Toole C, Cross S, Farnworth J. Efficient modelling of the structural response of submarine pressure hulls to underwater explosions. In *Warship 2017: Naval Submarines & UUVs, The Royal Institution of Naval Architects* 2017.
4. Bonnet M. *Boundary integral equation methods in solids and fluids*. John Wiley & sons . 1999.
5. Dominguez J. *Boundary elements in dynamics*. Elsevier Applied Science Publishers . 1993.
6. Gwinner J, Stephan EP. *Advanced boundary element methods*. Springer International Publishing . 2018.
7. Antes H. A boundary element procedure for transient wave propagations in two-dimensional isotropic elastic media. *Finite Elem. Anal. Des.* 1985; 1: 313 - 322.
8. Ha-Duong T. On retarded potential boundary integral equations and their discretisation. In: Springer Berlin Heidelberg. 2003 (pp. 301–336).
9. Abboud T, Nédélec JC, Volakis J. Stable solution of the retarded potential equations. *17th Annual Review of Progress in Applied Computational Electromagnetics* 2001: 146 - 151.
10. Aimi A, Diligenti M, Guardasoni C, Mazzieri I, Panizzi S. An energy approach to space–time Galerkin BEM for wave propagation problems. *Int. J. Numer. Meth. Engrg.* 2009; 80(9): 1196-1240.
11. Costabel M. Time-Dependent Problems with the Boundary Integral Equation Method. In: 2004.
12. Lubich C. Convolution quadrature and discretized operational calculus. I. *Numer. Math* 1988; 52: 129 - 145.
13. Lubich C. Convolution quadrature and discretized operational calculus. II. *Numer. Math* 1988; 52: 413 - 425.
14. Banjai L, Sauter S. Rapid solution of the wave equation in unbounded domains. *SIAM Journal on Numerical Analysis* 2009; 47(1): 227–249.
15. Betcke T, Salles N, Smigaj W. Overresolving in the Laplace domain for convolution quadrature methods. *SIAM J. Sci. Comput.* 2017; 39(1): A188 - A213.

16. Nieto Ferro A. *Nonlinear dynamic soil-structure interaction in earthquake engineering*. PhD thesis. École Centrale Paris, Paris, France; 2013.

17. Sayas FJ. *Retarded potentials and time domain boundary integral equations. a road map*. 50 of *Springer Series in Computational Mathematics*. Springer International Publishing . 2016.

18. Labarca I, Faria LM, Pérez-Arancibia C. Convolution quadrature methods for time-domain scattering from unbounded penetrable interfaces. *Proceedings of the Royal Society A* 2019; 475(2227): 20190029.

19. Chaillat S, Darbas M, Le Louer F. Fast iterative boundary element methods for high-frequency scattering problems in 3D elastodynamic. *J. Comput. Phys.* 2017; 341: 429 - 446.

20. Darbas M, Darrigrand E, Lafranche Y. Combining analytic preconditioner and fast multipole method for the 3-D Helmholtz equation. *J. Comput. Phys.* 2013; 236: 289-316.

21. Darve E. The fast multipole method: numerical implementation. *J. Comput. Phys.* 2000; 160: 195 - 240.

22. Fong W, Darve E. The black-box fast multipole method. *J. Comput. Phys.* 2009; 228(23): 8712 - 8725.

23. Bremer J, Gillman A, Martinsson PG. A high-order accurate accelerated direct solver for acoustic scattering from surfaces. *BIT Numer. Math.* 2013; 55: 367-397.

24. Ergin AA, Shanker B, Michielssen E. Fast evaluation of three-dimensional transient wave fields using diagonal translation operators. *J. Comput. Phys.* 1998; 146: 157–180.

25. Takahashi T, Nishimura N, Kobayashi S. A fast BIEM for three-dimensional elastodynamics in time domain. *Engrg. Anal. Bound. Elem.* 2004; 28: 165–180.

26. Jury EI. *Theory and application of the Z-transform method*. Krieger . 1973.

27. Banjai L, Messner M, Schanz M. Runge-Kutta convolution quadrature for the Boundary Element Method. *Comput. Meth. Appl. Mech. Engrg.* 2012; 245/246: 90 - 101.

28. Anderson TG, Bruno OP, Lyon M. High-order, dispersionless "fast-hybrid" wave equation solver. Part I: O(1) sampling cost via incident-field windowing and recentering. *SIAM Journal on Scientific Computing* 2020; 42(2): A1348-A1379.

29. Quarteroni A, Sacco R, Saleri F. *Numerical mathematics*. Springer . 2007.

30. Banerjee PK. *The boundary element methods in engineering*. McGraw-Hill. 2nd ed. 1994.

31. Bielak J, Maccamy RC. Symmetric finite-element and boundary integral coupling methods for fluid-solid interaction. *Quart. Appl. Math.* 1991; 49: 107 - 119.

32. Bonnet M, Maier G, Polizzotto G. Symmetric Galerkin boundary element methods. *Appl. Mech. Rev.* 1998; 51: 669 - 704.

33. Kallivokas LF, Juneja T, Bielak J. A symmetric Galerkin BEM variational framework for multi-domain interface problems. *Comp. Meth. Appl. Mech. Engrg.* 2005; 194: 3607 - 3636.

34. Hughes TJR. *The finite element method: linear static and dynamic finite element analysis*. Prentice-Hall . 1987.

35. Saad Y, Schultz M. GMRES: A generalized minimal residual algorithm for solving nonsymmetric linear systems. *SIAM J. Sci. Stat. Comput.* 1986; 7(3): 856 - 869.

36. Chaillat S. *Fast multipole method for 3-d elastodynamic boundary integral equations. Application to seismic wave propagation*. PhD thesis. École Nationale des Ponts et Chaussées, Paris, France; 2008.

37. Nishimura N. Fast multipole accelerated boundary integral equation methods. *Appl. Mech. Rev.* 2002; 55: 299 - 324.

38. Hackbusch W. A sparse matrix arithmetic based on H-matrix. Part I: Introduction to H-matrices. *Computing* 1999; 62: 89 - 108.

39. Chaillat S, Desiderio L, Ciarlet P. Theory and implementation of $\mathcal{H}$-matrix based iterative and direct solvers for Helmholtz and elastodynamic oscillatory kernels. *J. Comp. Phys.* 2017; 351: 165 - 186.

40. Junger MC, Feit D. *Sound, structures, and their interaction*. The MIT Press. 2nd ed. 1986.

41. Ohayon R, Soize C. *Structural acoustics and vibration*. Academic Press . 1998.

42. Baker BB, Copson ET. *The mathematical theory of huygens' principle*. Chelsea Publishing Company . 1950.

43. Abboud T, Nédélec JC, Zhou B. Méthode des équations intégrales pour les hautes fréquences. *Comptes rendus de l'Académie des sciences. Série 1, Mathématique* 1994; 318(2): 165–170.

44. Bruno OP, Geuzaine CA, Monro Jr JA, Reitich F. Prescribed error tolerances within fixed computational times for scattering problems of arbitrarily high frequency: the convex case. *Philosophical Transactions of the Royal Society of London. Series A: Mathematical, Physical and Engineering Sciences* 2004; 362(1816): 629–645.

45. Chandler-Wilde SN, Langdon S. A Galerkin boundary element method for high frequency scattering by convex polygons. *SIAM Journal on Numerical Analysis* 2007; 45(2): 610–640.

46. Loseille A. Chapter 10 - Unstructured mesh generation and adaptation. In: Abgrall R, Shu CW., eds. *Handbook of numerical methods for hyperbolic problems*. 18 of *Handbook of Numerical Analysis*. Elsevier. 2017 (pp. 263 - 302).

47. Chaillat S, Bonnet M, Semblat JF. A multi-level fast multipole BEM for 3-D elastodynamics in the frequency domain. *Comput. Meth. Appl. Mech. Engrg.* 2008; 197(49): 4233 - 4249.

48. Swisdak MM. Explosion Effects and Properties. Part II. Explosion Effects in Water. Tech. Rep. NSWC/WOL TR 76 - 116, Naval Surface Weapons Center; Dahlgren, Virginia: 1978.

49. Geers TL, Hunter KS. An integrated wave-effects model for an underwater explosion bubble. *J. Acoust. Soc. Am.* 2002; 111(4): 1584 - 1601.

50. Overpelt B, Nienhuis B, Anderson B. Free running manoeuvring model tests on a modern generic ssk class submarine (BB2). *Pacific International Maritime Conference, Sydney, Australia* 2015.

51. François S, Masoumi HR, Degrande G. A time domain coupled boundary element - finite element method for dynamic response of structures. *12th International Congress on Sound and Vibration* 2005.

52. Felippa CA, Park KC, Farhat C. Partitioned analysis of coupled mechanical systems. *Comput. Meth. Appl. Mech. Engrg.* 2001; 190(24): 3247 - 3270.

53. Soares Jr. D, Mansur WJ. An efficient time-domain BEM/FEM coupling for acoustic-elastodynamic interaction problems. *Comput. Model. Engng. Sci.* 2005; 8(2): 153 - 164.

54. Zhang AM, Yao XL. Interaction of underwater explosion bubble with complex elastic-plastic structure. *Appl. Math. Mech.* 2008; 29(1): 89 - 100.

55. Greengard L. *The rapid evaluation of potential fields in particle systems*. MIT Press . 1988.

56. Greengard L, Rokhlin V. A fast algorithm for particle simulations. *J. Comp. Phys.* 1987; 73: 325 - 348.

57. Ying L. A pedestrian introduction to fast multipole methods. *Science China Mathematics* 2012; 55(5): 1043 - 1051.

58. Epton MA, Dembart B. Multipole translation theory for the three-dimensional Laplace and Helmholtz equations. *SIAM J. Sci. Comput.* 1995; 16(4): 865 - 897.

59. Olver FWJ, Lozier DW, Boisvert RF, Clark CW. *NIST handbook of mathematical functions*. Cambridge University Press . 2010.

60. Iakovlev S. Influence of a rigid coaxial core on the stress-strain state of a submerged fluid-filled circular cylindrical shell subjected to a shock wave. *Journal of Fluids and Structures* 2004; 19(7): 957 - 984.